JOURNAL OF GEOPHYSICAL RESEARCH, VOL. 115, E06007, doi:10.1029/2009JE003499, 2010

Click Here for Full Article

An improved lunar gravity field model from SELENE and historical tracking data: Revealing the farside gravity features

K. Matsumoto,[1] S. Goossens,[1] Y. Ishihara,[1] Q. Liu,[1,2] F. Kikuchi,[1] T. Iwata,[3] N. Namiki,[4] H. Noda,[1] H. Hanada,[1] N. Kawano,[1,2] F. G. Lemoine,[5] and D. D. Rowlands[5]

Received 26 August 2009; revised 17 November 2009; accepted 13 January 2010; published 16 June 2010.

[1] A new spherical harmonic solution of the lunar gravity field to degree and order 100, called SGM100h, has been developed using historical tracking data and 14.2 months of SELENE tracking data (from 20 October 2007 to 26 December 2008 plus 30 January 2009). The latter includes all usable 4-way Doppler data collected which allowed direct observations of the farside gravity field for the first time. The new model successfully reveals farside features in free-air gravity anomalies which are characterized by ring-shaped structures for large impact basins and negative spots for large craters. SGM100h produces a correlation with SELENE-derived topography as high as about 0.9, through degree 70. Comparison between SGM100h and LP100K (one of the pre-SELENE models) shows that the large gravity errors which existed in LP100K are drastically reduced and the asymmetric error distribution between the nearside and the farside almost disappears. The gravity anomaly errors predicted from the error covariance, through degree and order 100, are 26 mGal and 35 mGal for the nearside and the farside, respectively. Owing to the 4-way Doppler measurements the gravity coefficients below degree and order 70 are now determined by real observations with contribution factors larger than 80 percent. With the SELENE farside data coverage, it is possible to estimate the gravity field to degree and order 70 without applying any a priori constraint or regularization. SGM100h can be used for global geophysical interpretation through degree and order 70.

Citation: Matsumoto, K., et al. (2010), An improved lunar gravity field model from SELENE and historical tracking data: Revealing the farside gravity features, *J. Geophys. Res.*, *115*, E06007, doi:10.1029/2009JE003499.

1. Introduction

[2] Study of the lunar gravity field plays an important role in understanding the structure and the evolution of our celestial neighbor. Many efforts have been made to develop lunar gravity field models since the first lunar orbiter Russian Luna 10 mission in 1966 [*Akim*, 1966]. The Luna 10 was followed by a series of U.S. Lunar Orbiter missions (LO-I to LO-V) with various orbital inclinations and eccentricities. By differentiating the LO-V Doppler residuals, *Muller and Sjogren* [1968] obtained the acceleration along the line-of-sight (LOS) direction between the spacecraft and tracking station, and found large positive gravity anomalies within the ringed lunar maria basins which are called "mass concentrations" (mascons). The landmark solution of *Muller and Sjogren* [1968] was followed by many solutions of the global lunar gravity field using a spherical harmonic expansion. These include the solutions by *Bills and Ferrari* [1980] (a degree 16 × order 16 model) and *Konopliv et al.* [1993] (a 60 × 60 model, LUN60D) which were developed by using the tracking data from Apollo 15 and 16 subsatellites in addition to the Lunar Orbiter data. The LUN60D model had excellent performance in terms of its root mean square (RMS) fit to the tracking data, but high-degree terms have excessive spurious power when the gravity anomalies are mapped onto the lunar surface. *Lemoine et al.* [1997] developed a 70 × 70 model (GLGM-2) by further including U.S. Clementine tracking data. Since Clementine had a polar orbit with relatively high periapsis height of about 400 km, the data provided the strongest constraints on the global long wavelength gravity signature.

[3] New tracking data stream from U.S. Lunar Prospector (LP) provided much improved knowledge of the lunar gravity field, which resulted in a series of LP gravity models [*Konopliv et al.*, 1998, 2001; *Konopliv and Yuan*, 1999]. LP

[1]RISE Project, National Astronomical Observatory of Japan, Mizusawa, Oshu, Iwate, Japan.
[2]Now at Shanghai Astronomical Observatory, Shanghai, China.
[3]Japan Aerospace Exploration Agency, Sagamihara, Japan.
[4]Planetary Exploration Research Center, Chiba Institute of Technology, Narashino, Japan.
[5]Planetary Geodynamics Laboratory, Solar System Exploration Division, NASA Goddard Space Flight Center, Greenbelt, Maryland, USA.

Copyright 2010 by the American Geophysical Union.
0148-0227/10/2009JE003499

remained in a near circular polar orbit at a mean altitude of 100 km during the 1 year nominal mission, and in the subsequent 6 month extended mission the spacecraft was lowered to an average altitude of 30 km to obtain higher resolution gravity. The LP gravity models such as LP100K and LP150Q (the latest LP model with one-step inversion process, available at http://pds-geosciences.wustl.edu/lunar01/lp-l-rss-5-gravity-v1/lp_1001/sha/jgl150q1.sha), which include all the LP tracking data as well as the historical data, successfully identified many fine-scale gravity signatures in the nearside.

[4] However, the modeling of farside gravity features was of limited geophysical value, because these models were based on direct tracking data of the spacecraft from Earth-based tracking stations. The fact that the Moon is in the state of synchronous rotation made it difficult to obtain detailed information of the "global" lunar gravity field. A direct tracking data stream of a low-altitude lunar satellite in circular orbit will leave about 2/3 of the farside hemisphere unobserved. In such a situation, when determining the gravity coefficients in terms of spherical harmonics in a least squares sense, some kind of regularization is necessary to avoid numerical instabilities which stem from the highly inhomogeneous spatial data density. Because of its simplicity, the common practice is to constrain each coefficient toward zero with an uncertainty given by Kaula's rule of thumb [*Kaula*, 1966];

$$\left\{\sigma(\overline{C}_{nm}), \sigma(\overline{S}_{nm})\right\} = \beta \times 10^{-4}/n^2 \tag{1}$$

where $\sigma(\overline{C}_{nm})$ and $\sigma(\overline{S}_{nm})$ are errors of normalized selenopotential coefficients of degree n and order m (see equation (2) and (3) for definition), and β is a scaling constant. A variant constraint is suggested by *Konopliv and Sjogren* [1994] for the case of Venus where surface gravity is geographically constrained, not the individual coefficients, in places where no direct measurements are available. This technique proved to be unsuccessful for the Moon because the farside gap is too large [*Konopliv et al.*, 2001]. The Kaula-type signal constraint acts as a gravity field smoother and results in good data fit over the nearside, but the farside gravity field is almost meaningless as is clearly shown by *Floberghagen et al.* [1999]. Another difficulty with the application of the power constraint is the selection of the appropriate value of β. For the Earth, independent surface gravity measurements constrain the amplitude of the power spectrum, whereas no such information is available for the Moon. *Kaula* [1963] predicted β of the Moon to be 3.57 by using a scaling law based on the assumption that the Moon has similar strength to the Earth, but the choice of β value is up to gravity modelers. For example, *Lemoine et al.* [1997] applied β = 1.5 whereas *Konopliv et al.* [2001] preferred β = 3.6. Thus, the GLGM-2 model underestimates the expected power in the lunar gravity field at short wavelengths (beyond degree 20), but this is the consequence of aiming at producing a model which is more suitable for geophysical studies of the Moon in terms of basin-scale features by attenuating the artifacts from the high-degree terms seen in LUN60D.

[5] Even if one produced a global lunar gravity solution using the power constraint, the error in the farside is naturally large because there are no direct observations. Thus other, more locally concentrated representation forms become suitable for describing the well-sampled parts of the lunar gravity field. *Sugano and Heki* [2004] produced a high-resolution nearside gravity map by solving for discrete mass anomalies without placing any a priori power law constraint, to exhaust the gravity information contained in the LP Doppler tracking data. *Han* [2008] solved for localized spherical harmonics to represent high-resolution gravity field over four selected spherical cap regions on the nearside. The approach of *Han et al.* [2009] was to make use of a power low constraint which is effective only within the farside and the limb region. They were able to get higher correlation with topography in the nearside by using these techniques. However, the large farside data gap remained as a major challenge for global lunar gravity field modeling.

[6] The Japanese lunar exploration project SELENE (SELenological and ENgineering Explorer) has filled in the farside data gap by a high-low satellite-to-satellite Doppler tracking. The new farside tracking by way of the SELENE relay satellite is called 4-way Doppler [*Namiki et al.*, 1999]. *Namiki et al.* [2009] reported a lunar gravity field model complete up to degree and order 90, which included 25,005 4-way Doppler observations. The new model, named as SELENE Gravity Model version d (SGM90d), clearly resolved ring-shaped farside gravity signatures within major impact basins. *Namiki et al.* [2009] proposed a new classification of the basins on the farside and the limb based on the magnitude of central gravity high in free-air anomaly compared to that in Bouguer anomaly.

[7] In this paper we present a successor model to SGM90d, a 100 × 100 model designated SGM100h, which is based on historical tracking data and 14.2 months of SELENE tracking data including all the usable 4-way Doppler data. The number of 4-way Doppler data used in this study was 78,004, which is more than three-fold compared to that was included in SGM90d (25,005). The paper is organized as follows. Section 2 addresses the mission instruments, satellite orbits, and the tracking data of SELENE which characterize the gravity mission. Section 3 describes the details of data processing to derive a spherical harmonic solution of the lunar gravity field. The signature and quality of the gravity model are addressed in section 4 by comparing it with other gravity models and a SELENE-derived lunar topography model, and a summary is given in section 5.

2. SELENE Gravimetry

2.1. Satellites and Mission Instruments

[8] SELENE consists of three satellites; a main satellite, a relay subsatellite, and a VLBI (Very Long Baseline Interferometry) subsatellite. Each of them has a Japanese nickname Kaguya, Okina, and Ouna, respectively. Hereinafter the main satellite is referred to as Kaguya, but the relay and VLBI subsatellites are referred to as Rstar and Vstar, respectively, to be consistent with the prelaunch nomenclature. Kaguya is a three-axis attitude controlled satellite, whereas Rstar and Vstar are spin-stabilized small satellites. Each of the subsatellites has an octagonal prism body which measures 1 m by 1 m by 0.65 m, and a total mass of about 45 kg. The mass of Kaguya at entry of mapping orbit was 2107 kg.

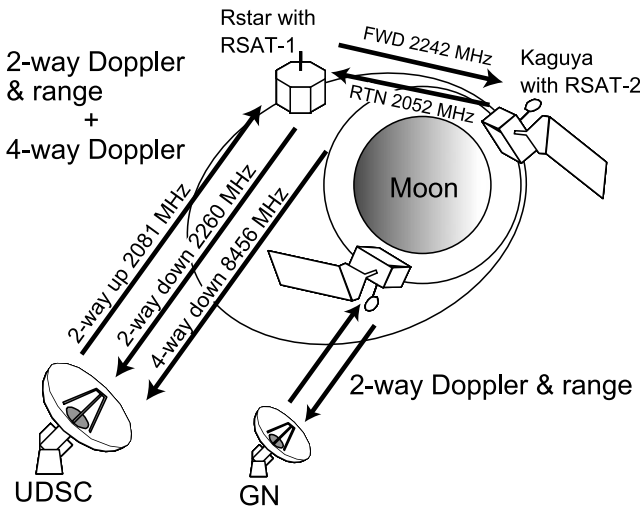

Figure 1. A schematic figure showing the concept of the RSAT mission to obtain 4-way Doppler data in the farside of the Moon. FWD and RTN indicate the forward and return links between Rstar and Kaguya, respectively.

[9] Two mission instruments play important roles in SELENE gravimetry, i.e., RSAT, a satellite-to-satellite Doppler tracking system [*Namiki et al.*, 1999] and VRAD, artificial radio sources for VLBI [*Hanada et al.*, 2008]. The RSAT consists of two communication instruments, one is called RSAT-1 installed on Rstar, and the other is called RSAT-2 on Kaguya. RSAT-1 controls 2-way Doppler and range measurements as well as the forward part of 4-way Doppler measurement, while RSAT-2 serves as a transponder for the return part of 4-way Doppler (see Figure 1). An S-band signal of 2081 MHz is uplinked from the Earth-based tracking station, Usuda Deep Space Center (UDSC) of JAXA with a 64 m antenna, to RSAT-1 which returns a downlink signal of 2260 MHz to UDSC. Kaguya and Vstar have the similar transponders for 2-way Doppler and range measurements. After receiving the uplink signal from UDSC, RSAT-1 transmits another S-band coherent signal of 2242 MHz to Kaguya. RSAT-2 on Kaguya receives the forwarded signal and transmits a return signal of 2052MHz to RSAT-1 which then transmits to UDSC an X-band coherent signal of 8456 MHz which is generated by mixing the 4-way return signal and the 2-way downlink signal. Thus, the 2-way observables for Rstar are simultaneously obtained when the 4-way Doppler measurements of Kaguya are performed.

[10] Two pairs of S-band patch omnidirectional antennas with conical beams are installed on both the upper and lower decks of Rstar, which are used for establishing the middle part of the 4-way link (the forward and the return links). The relative position of Rstar with respect to Kaguya geometrically determines which of the upper or lower deck antennas should be used. Each of the paired antennas, one for transmitting and the other for receiving, are placed in axial symmetry around Rstar's spin axis to reduce the spin-induced Doppler noise. The 4-way Doppler measurement achieves direct tracking of Kaguya as through high-low satellite-to-satellite tracking, which is of great importance in terms of filling the farside data gap that existed before SELENE. Rstar and Vstar are also equipped with radio sources called VRAD-1 and VRAD-2, respectively, which emit three carrier waves in S-band (2212, 2218, 2287 MHz) and one in X-band (8456 MHz) for the purpose of differential VLBI measurements. A more detailed description of the properties of the mission instruments is given by *Iwata et al.* [2001].

2.2. Satellite Orbits

[11] The SELENE spacecraft were launched on 14 September 2007. After entering lunar orbit on 4 October 2007, Rstar and Vstar were released from Kaguya on 9 October 2007 and 12 October 2007, respectively. The initial orbit of Rstar was elliptical with a periapsis height of 120 km and an apoapsis height of 2395 km, while Vstar was inserted into a less elliptical orbit with a periapsis height of 129 km and an apoapsis height of 792 km. Kaguya reached its nominal orbit with mean altitude of 100 km on 20 October 2007. The three satellites are coplanar with an initial inclination of about 90°. The orbital periods of Kaguya, Vstar, and Rstar are about 2, 2.5, and 4 hours, respectively.

[12] Since Rstar and Vstar are free fliers which do not perform any propulsive maneuvers, their orbits evolve primarily due to the influence of the gravity field of the Moon and the third body perturbation of the Earth and, to a lesser extent, due to solar radiation pressure. The orbital perturbation due to the Earth's gravity is relatively larger for Rstar than for Vstar because of Rstar's higher mean altitude. The eccentricity of the Rstar orbit varied with time, being affected mainly by the gravity of the Earth, from the initial value of 0.38 to the minimum value of 0.25 on 22 May 2008. The eccentricity then increased up to the final maximum value of 0.42 on 12 February 2009, when Rstar finished its mission by colliding with the lunar surface. The argument of periapsis of Rstar almost monotonically decreased from the initial value of 135° to the final value of 28°. Thus the apoapsis of Rstar was always on the southern hemisphere, which resulted in better 4-way Doppler coverage in that hemisphere (see Figure 2).

[13] The altitude of Kaguya was maintained in the range of 100 ± 30 km by periodic altitude maintenance maneuvers conducted about every 2 months. Kaguya periodically fired its thrusters to desaturate its momentum wheels, which absorb angular momentum caused by disturbance torques acting on the satellite. The angular momentum desaturation (AMD) events occurred about every 12 hours until one of the four momentum wheels malfunctioned on 23 July 2008. The AMD interval was then about 6 hours on average from 23 July 2008 to 26 December 2008 when another wheel was stopped due to anomalous drag. After this date, the attitude of Kaguya was mainly controlled by the thrusters and the altitude gradually decreased. The arc length (interval of orbit solution) of Kaguya is defined in terms of the AMD interval as described in section 3.1. The operation of Kaguya came to an end on 10 June 2009, by a controlled impact on the lunar surface. The tracking of Vstar stopped on 29 June 2009, by turning off the transponder and the radio source.

2.3. SELENE Tracking Data

[14] Four types of satellite tracking data are acquired in SELENE mission, i.e., (1) 2-way Doppler for the three satellites, (2) 2-way range for the three satellites, (3) 4-way

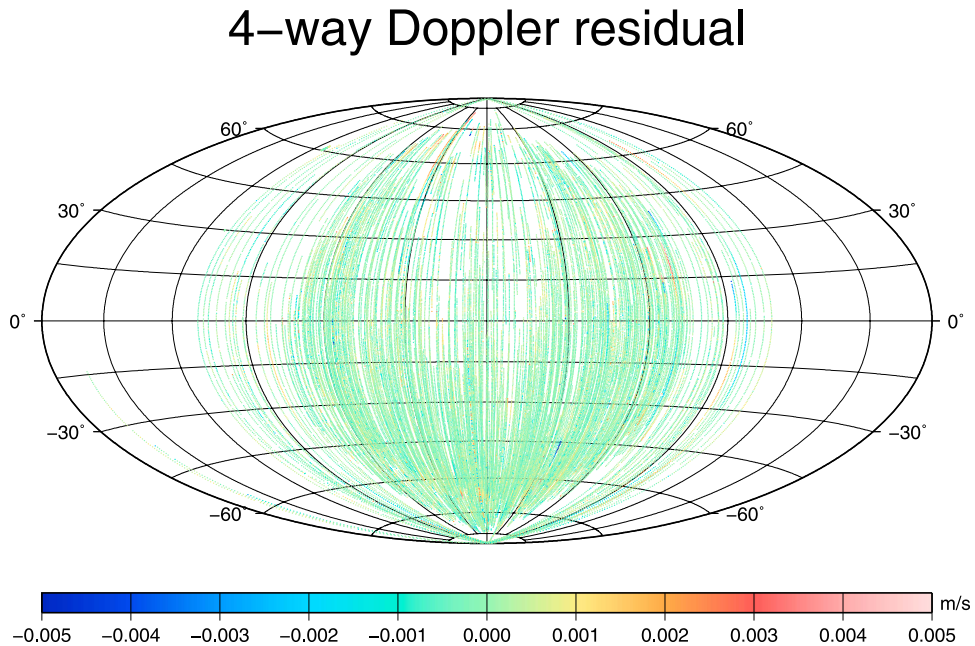

Figure 2. A map showing the selenographical distribution of the postfit residual of 4-way Doppler measurements, which also shows the data coverage achieved by RSAT mission of SELENE. The map is centered on 180° E longitude.

Doppler for Kaguya by way of Rstar, and (4) differential VLBI between Rstar and Vstar. The 2-way Doppler data for Kaguya generally came from Uchinoura 34 m antenna and Ground Network (GN) stations of JAXA with antennas of 10 to 18 m diameters. The GN consists of five domestic stations located at Katsu'ura, Masuda, Okinawa, and three oversea stations of Maspalomas (Canary Islands), Perth (Australia), and Santiago (Chile). The station coordinates are summarized in Table 1. The global distribution of GN stations provided almost continuous 2-way Doppler tracking of Kaguya in the nominal mission phase which continued until the end of October, 2008. However, the 2-way Doppler tracking by the oversea GN stations was suspended in the extended mission phase which started on 1 November except for the latter half of December 2008. No 2-way range data were collected at the GN. The 2-way Doppler and range data for Kaguya were sometimes acquired at UDSC, but in smaller quantity compared to the data from the GN stations. The 4-way Doppler data were collected at UDSC.

[15] Rstar and Vstar were tracked by UDSC using 2-way Doppler and range and also by four domestic stations of Japanese VERA project (Mizusawa, Ogasawara, Iriki, and Ishigaki) [*Kobayashi et al.*, 2003] using differential VLBI. The VERA antenna time assigned to SELENE was about 100 hours per month on average. The accuracy of the differential phase delay from VERA stations is estimated to be a few pico seconds [*Kikuchi et al.*, 2009]. For more precise orbit determination for Rstar and Vstar with longer baselines, there have been two spans of international VLBI tracking campaigns in which four additional stations located in Shanghai, Urumqi (China), Hobart (Tasmania), and Wettzell (Germany) participated. The span of each international campaign was 1 month. Although the differential VLBI data are not yet included in the lunar gravity field model of this study, a contribution of VLBI data from the VERA stations to improving orbit consistency of Rstar and Vstar has already been confirmed by *Kikuchi et al.* [2009].

[16] Since the three SELENE satellites have different orbital periods, the visibility conditions are different day by day, which makes the tracking scheduling somewhat complicated. When Kaguya is visible from UDSC, the antenna is in principle oriented to Kaguya in order to transfer scientific data down to the station. We had opportunities for 2-way tracking of subsatellites or 4-way tracking of Kaguya only when Kaguya was in lunar occultation (or on the farside). Among the tracking data of subsatellites by UDSC, 4-way Doppler was given the highest priority because of its importance of filling the farside data gap. During the UDSC antenna time allocated to the subsatellites, 4-way Doppler data were collected whenever the satellites geometry and antenna beam pattern allowed the 4-way link. After determining the time span for 4-way Doppler, we still had room to choose which 2-way measurement for Rstar or Vstar was carried out. The Vstar 2-way observation was

Table 1. Coordinates and Antenna Diameters of the Tracking Stations Used for SELENE Doppler and Range Measurements[a]

Station Name	Diameter (m)	Earth Fixed Coordinates (km)		
		X	Y	Z
Usuda (UDSC)	64	−3855.35536	3427.42764	3740.97134
Uchinoura (USC)	34	−3586.22864	4114.10392	3290.22477
Katsu'ura (KTU1)	10	−4014.22236	3332.57672	3656.96072
Katsu'ura (KTU2)	13	−4014.28771	3332.75298	3656.66283
Okinawa (OKN1)	10	−3508.85429	4507.25017	2828.62948
Okinawa (OKN2)	18	−3508.94929	4507.16234	2828.63533
Masuda (MSD1)	10	−3607.55177	4148.00187	3223.67825
Maspalomas (MSP1)	10	5439.08908	−1522.18448	2953.58420
Perth (PRT1)	10	−2368.73103	4880.88466	−3342.40690
Santiago (SNT1)	10	1769.81400	−5044.59533	−3468.24684

[a]The reference frame is WGS84.

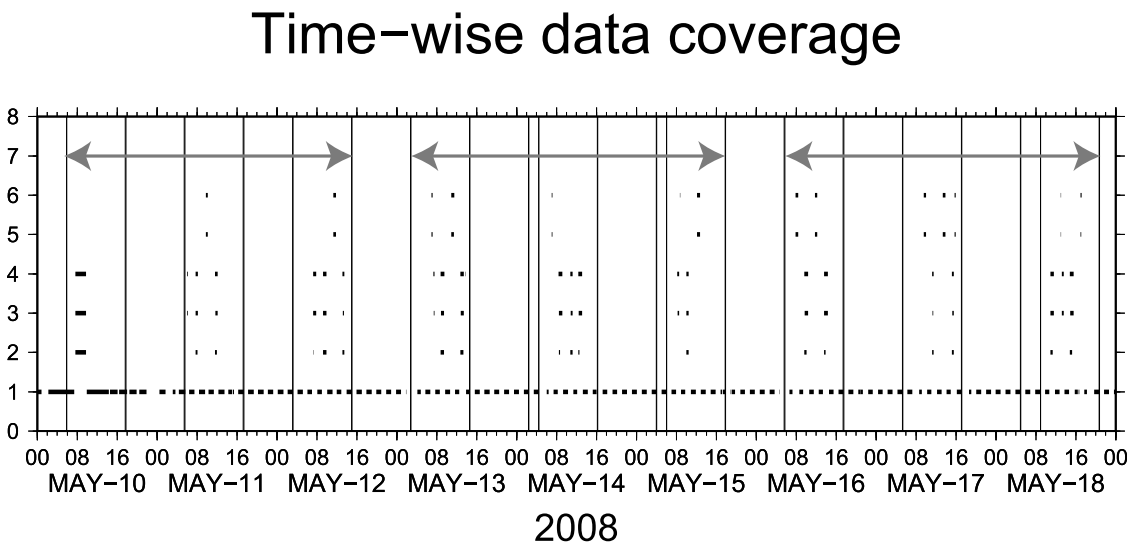

Figure 3. An example of time-wise data coverage of SELENE tracking data from 10 to 18 May 2008. The horizontal axis indicates the universal time. The vertical axis corresponds to data category; (1) 2-way Doppler for Kaguya, (2) 4-way Doppler, (3) 2-way range for Rstar, (4) 2-way Doppler for Rstar, (5) 2-way range for Vstar, (6) 2-way Doppler for Vstar. The 2-way Doppler data of Kaguya were collected at the globally distributed GN stations, while other types of the data were collected at UDSC in Japan. No 2-way range data for Kaguya were obtained by UDSC in this period. Vertical solid lines indicate the timings of the angular momentum desaturation events. Most of the breaks in the Kaguya 2-way Doppler data acquisition corresponds to the occultation of Kaguya, during which Rstar or Vstar is tracked. Gray arrows indicate arc boundaries of Rstar which are used for orbit analysis. Tracking data of Rstar on 10 May were obtained by the optional operation during face-on orbit configuration.

preferentially chosen when there was a chance for occultation observations using the radio signal from Vstar to detect the lunar ionosphere [*Imamura et al.*, 2008] or for same-beam VLBI observations [*Kikuchi et al.*, 2009]. Some exceptions for the general tracking rule of UDSC were permitted, i.e., tracking of the subsatellites even in so-called face-on orbit geometry in which the spacecraft fly over the lunar limb region without occultation. We obtained some 4-way Doppler data over the limb so that the radial sensitivity of the 4-way Doppler observable would place additional constraints on the lunar gravity field in this region of the Moon, which from conventional Earth-based tracking is only observed with a face-on orbit geometry. We also had opportunities for tracking of the subsatellites when telemetry for battery health checks are collected by UDSC during face-on orbits. Figure 3 shows an example of the time-wise coverage of the SELENE Doppler and range data from 10 to 18 May 2008. It is clear that the amount of tracking data for Rstar and Vstar is less than that for Kaguya. This is because of the above mentioned limited availability of the UDSC for the subsatellites compared to the continuous availability of the GN stations for Kaguya.

[17] The spacecraft spin introduces two separate effects into the Doppler data. The first is a bias and the second is a sinusoidal signature due to an offset of the antenna phase center from the spacecraft spin axis [*Montenbruck and Gill*, 2000; *Konopliv et al.*, 2001]. The former effect can be absorbed by a Doppler bias introduced in orbit determination process, although a careful attention should be paid when antennas are switched between the upper and lower decks within a 4-way Doppler pass (see section 3.1). The latter effect is also evident in 2-way Doppler data for Rstar and Vstar, but is more problematic for 4-way Doppler because the patch omnidirectional antennas have an offset of 45 cm from the Rstar spin axis. Despite the symmetrical installation of the antennas, the spin-induced noise is unavoidable due to the nonzero round-trip travel time of the radio wave between Rstar and Kaguya. Furthermore, irregularities in the antenna phase pattern, which means deviations of the wavefront from perfect sphericity, impose on the Doppler frequency periodic noise with the spin frequency and its higher-order harmonics [*Ping et al.*, 2000; *Liu et al.*, 2004]. By analyzing the spin-induced fluctuations which appeared in the raw 10 Hz 2-way Doppler data, the initial spin frequencies of Rstar and Vstar are found to be 0.1833 Hz and 0.1875 Hz, respectively [*Liu et al.*, 2010]. They are higher than the highest frequency of the expected gravity signal of interest which is about 0.03 Hz corresponding to half wavelength of spherical harmonic field at degree 100 when the Kaguya orbital velocity of 1.6 km/s is assumed. In order to avoid the spin-induced high-frequency noise from contaminating our gravity analysis through aliasing, we have developed a digital low-pass filter which keeps the gravity signal intact [*Liu et al.*, 2010]. The Doppler data collected at UDSC had a time interval of 0.1 seconds, and all the Doppler data related to the subsatellites, including the 4-way Doppler, were passed through the digital low-pass filter and then integrated to an interval of 10 seconds. Also integrated over 10 seconds are 2-way Doppler data of Kaguya collected at the GN stations with 1 second interval, where no low-pass filtering is needed because Kaguya is not a spin satellite. The

2-way range data were acquired with 1 second interval, but to balance things out, the data are also compressed to an interval of 10 seconds. The span of the SELENE data analyzed in this paper is from 20 October 2007 to 26 December 2008, plus 30 January 2009, which includes all the usable 4-way Doppler data that were obtained with the wheel control mode of Kaguya. The 4-way Doppler data on 30 January 2009 were specially obtained in one of the data gap regions that remained at that time, with three reaction wheels switched on, even though one of them was not in good condition, by carefully monitoring the wheel drag. The altitude of Kaguya on this day was about 60 km which is lower than the nominal altitude.

3. Derivation of Spherical Harmonic Solutions

3.1. Processing of the SELENE Tracking Data

[18] Processing of the tracking data for precise orbit determination and gravity field estimation is done with the GEODYN II [*Pavlis et al.*, 2009] and SOLVE [*Ullman*, 2002] software. The estimated parameters concerning the orbit determination and the gravity field estimation are often conventionally separated into two parts: one concerning the so-called arc parameters, and the other concerning so-called common (or global) parameters. The tracking data are divided into short continuous spans of time over which the orbit is estimated, otherwise errors tend to build up when long spans of time are integrated, due to imperfect force modeling, imperfect knowledge of the initial state vectors and other parameters. If the errors at the end of the arc become too large, the problem cannot be successfully linearized for least squares estimation. These spans are called arcs, and parameters such as the initial state vectors, measurement biases, solar radiation pressure coefficients, being valid for that particular arc, are called arc parameters. On the other hand, parameters such as the gravity coefficients, lunar gravitational constant GM, Love numbers, being the same for all combined arcs, are called common (or global) parameters. Since the equations of motion of spacecraft are nonlinear, the arc parameters are computed through numerical iteration. Once these are converged so that the orbit fits the data, the normal matrix for both arc and common parameters is generated per arc. The portion of common parameters only can be combined over all the arcs using partitioning technique [e.g., *Kaula*, 1966] and then inverted to solve for the common parameters. Here, GEODYN II is used as a normal matrix generator, and SOLVE is used for combining the normal matrices and inverting the combined matrix. GEODYN II has been specifically modified for including the interplanetary 4-way Doppler data.

[19] Since the 4-way Doppler links Kaguya and Rstar, it contains orbit information of the two satellites. Thus the processing of 4-way Doppler data requires simultaneous orbit determination of Kaguya and Rstar and we took the following 5 steps for precise orbit determination.

[20] (1) Fit Kaguya orbit to 2-way Doppler data and, when available, 2-way range data. The arc boundaries were determined by the timings of the AMD events, which were on average every 12 hours until 23 July 2009, and about every 6 hours afterward. Longer arcs of Kaguya could be used by modeling the accelerations induced by the AMD's. However, we did not integrate through the AMD events to prevent the artificial accelerations from corrupting our gravity estimation.

[21] (2) Reject bad 2-way Doppler data for Rstar. As described in section 2.3, 2-way Doppler data are also collected during 4-way Doppler measurements. It was often required to "sweep" the uplink frequency to get RSAT-2 locked to the signal so that the coherent links are established. Since the reference frequency drifts, it can be treated as ramped Doppler, but this is not included in our observation modeling. Furthermore, since the sweeping generally ended only in a few minutes, these 2-way Doppler data were manually deleted from the orbit and gravity analysis. This is done by looking at a timing table of the sweeping and also checked by confirming that no abnormally large 2-way Doppler residuals remain. The residuals are obtained by propagating the orbit, i.e, without estimating any arc parameters, by assuming that the spacecraft's initial state vectors and the force models are accurate enough to find the extreme outliers.

[22] (3) Fit Rstar orbit to 2-way Doppler and range data. The arc length of Rstar is set to be longer than that of Kaguya, by which we seek more geometrical sensitivity and more tracking data to obtain a more stable orbit. The mean arc length for Rstar is 2.6 days, compared to 12 hours used for SGM90d.

[23] (4) Reject bad 4-way Doppler data. This is done by the similar procedure to (2), but with Kaguya and Rstar combined. The converged orbits of Kaguya from (1) and those of Rstar from (3) are used to get the arc parameters for these setups. Since the arc length of Rstar is longer than that of Kaguya, these setups include multiple arcs of Kaguya. For example, within the Rstar arc starting at 05:59 May 10, 2008 UT and ending at 14:51 May 12, 2008 UT, five Kaguya arcs are included (see Figure 3) among which three arcs contain 4-way Doppler data. Each of the Kaguya arcs is apparently treated as an arc of individual satellite, by internally assigning different satellite ID to each of the virtual satellites.

[24] (5) Fit the orbits of Kaguya and Rstar to all the 2-way and 4-way data through several iterations until they are converged.

[25] The data are processed with a full-scale modeling of both the forces and the measurement link. The DE421 ephemeris [*Williams et al.*, 2008] is used for the computation of the third-body perturbations, as well as for the definition of the librations and lunar coordinate system. For Rstar and Vstar solar radiation pressure is modeled with a cannonball model and includes a scaling coefficient for each arc, C_R. The scaling coefficient is also estimated for each arc of Kaguya, but the complex shape of the spacecraft is taken into account by modeling it as a set of flat plates following *Marshall and Luthcke* [1994] and *Luthcke et al.* [1997]. The model consists of 6 plates that make up the spacecraft bus, and two plates that make up the solar panel (front and back). Kaguya's attitude in inertial space is described by quaternion information. From this attitude information, the solar incidence angle can be computed, and together with material properties, the solar radiation pressure force is computed following *Milani et al.* [1987]. The solar panels are assumed to be always pointing toward the Sun. Albedo was not included, and neither were self-shadowing effects, because

Table 2. Summary of Tracking Data and Arc Lengths Used in the Gravity Analysis

Satellite	Mean Arc Length	Data Type	Amount	Data Weight	Post-Fit Residual
SELENE Kaguya	12 hours[a]	4-way Doppler	78,004	1 mm/s	0.48 mm/s
		2-way Doppler	1,786,747	1, 2 mm/s	0.77 mm/s
		UDSC, GN			
		2-way range	62,438	5 m	0.82 m
SELENE Rstar	2.6 days	2-way Doppler	159,225	1 mm/s	0.50 mm/s
		2-way range	150,470	5 m	1.58 m
SELENE Vstar	2.4 days	2-way Doppler	42,502	1 mm/s	0.18 mm/s
		2-way range	35,567	5 m	1.03 m
LO-I	12 hours	3-way Doppler	3,867	4.5 mm/s	3.81 mm/s
		2-way Doppler	36,735	4.5 mm/s	4.38 mm/s
LO-II	12 hours	3-way Doppler	5,370	4.5 mm/s	4.13 mm/s
		2-way Doppler	42,376	4.5 mm/s	2.77 mm/s
LO-III	12 hours	3-way Doppler	1,957	4.5 mm/s	1.31 mm/s
		2-way Doppler	15,175	4.5 mm/s	1.25 mm/s
LO-IV	12 hours	3-way Doppler	1,780	4.5 mm/s	8.13 mm/s
		2-way Doppler	19,390	4.5 mm/s	5.17 mm/s
LO-V	12 hours	3-way Doppler	2,260	4.5 mm/s	3.38 mm/s
		2-way Doppler	13,397	4.5 mm/s	2.76 mm/s
Apollo 15 ss	8 hours	3-way Doppler	16,522	4.5 mm/s	1.42 mm/s
		2-way Doppler	28,986	4.5 mm/s	1.12 mm/s
Apollo 16 ss	8 hours	3-way Doppler	15,584	4.5 mm/s	3.58 mm/s
		2-way Doppler	15,459	4.5 mm/s	3.99 mm/s
Clementine	2 days	2-way Doppler	354,020	3 mm/s[b]	2.83 mm/s
		2-way range	5,091	6 m	2.00 m
Lunar Prospector[c]	2 days	2-way Doppler	3,155,182	2 mm/s	0.65 mm/s
		2-way range	430,414	4 m	0.83 m
SMART-1	15 hours	2-way Doppler	35,023	10 mm/s	0.62 mm/s

[a]6 hours after 23 July 2008.
[b]10 mm/s for Pomonkey.
[c]Only nominal mission data.

they have minor impact on the current orbit determination. These effects can be included in future refinements. In particular the albedo will be more important when LP extended mission data are incorporated. Kaguya has a high-gain antenna through which the spacecraft is tracked. This antenna was not taken into account in the solar radiation pressure model, but since it has an offset from the center of mass, this offset was taken into account in the measurement model, again using Kaguya's attitude in inertial space, to correctly model the location of the phase center. Including this offset decreased the tracking data residuals, and took out some systematic signals in the residuals coming from the motion of Kaguya.

[26] We have had progressive updates for SGM series; later models generally include more SELENE data and/or have higher expansion degree. Starting from LP75G [*Konopliv et al.*, 1998] as a priori model, we developed SGM90d. It was then used as the a priori model for SGM100g, which was based on an analysis procedure similar to the one described in this paper, but with slightly less amount of SELENE tracking data until the end of October 2008 (the nominal mission period) and the solar radiation pressure model for Kaguya was a simple cannon-ball. The a priori gravity field for this study was chosen to be SGM100g. The tidal force of the Earth and Sun on the Moon changes the gravity field; this is modeled with a degree 2 potential Love number k_2 with its initial value of 0.0213 [*Goossens and Matsumoto*, 2008] and it is estimated together with the gravity coefficients. The measurement link is corrected for media and relativistic effects within the processing software. Displacements on stations include solid Earth tides, pole tide loading and ocean loading per site. Estimated parameters for orbit determination are the state vector at epoch, the C_R coefficient, and measurement biases per pass on Doppler and range data to absorb further mis-modeling errors [e.g., *Lemoine et al.*, 1997]. Empirical accelerations were not estimated for SELENE because the relatively short arc lengths resulted in good data fits (see Table 2). However, arcs longer than one week would require either the application of empirical accelerations to absorb unmodeled effects, or better modeling of nonconservative forces.

[27] It is necessary to estimate separate 4-way Doppler biases when the pair of omnidirectional antennas are switched between the upper and lower decks within a single 4-way pass. As is shown by, e.g., *Liu et al.* [2004], rotation of a patch antenna introduces a bias in Doppler frequency. Since the direction of the rotation is opposite when seen from each of the antennas on different (upper or lower) decks, the effect is doubled when the switching occurs. The induced offset in the Doppler frequency due to the switching is thus $\delta f = 2 \times f_{spin} \times (1 + 270/295)$, where f_{spin} is the spin rate of Rstar in rev/s and 270/295 is the turn-around ratio of RSAT-2. Substituting 0.1833 to f_{spin} leads to a bias offset of δf = 0.702 Hz. Since the frequencies for the forward and the return links are different, it is difficult to precisely convert the δf to velocity. When we use, however, the midfrequency between 2242 and 2052 MHz (i.e., 2147 MHz) as a rough measure, the δf corresponds to a bias jump of 49 mm/s. During the RSAT mission period, thirteen of such switches were done, depending on the relative geometry of Kaguya and Rstar. If only one 4-way

Doppler bias was estimated for the pass, the spike-like jump of about 50 mm/s in the Doppler data resulted in a false gravity signature with concentric highs and lows in the modeled gravity field. Thus it is necessary to estimate independent biases for 4-way Doppler data taken by the antennas on the upper and lower decks, respectively. The bias jumps are also calculated from the pairs of two 4-way Doppler biases for the upper and lower antennas which are estimated through the orbit determination process. The mean value of the jumps is 51.1 mm/s with RMS of 0.9 mm/s, which is close to the theoretical prediction.

[28] The 2-way tracking data of Vstar until 31 August 2008 are separately processed with a mean arc length of 2.4 days. Although not all the data are included yet, the contribution from Vstar 2-way tracking data is limited due to its smaller amount of data. The importance of Vstar tracking will be enhanced when differential VLBI data are included in the gravity estimation, in particular for the low degree coefficients [*Matsumoto et al.*, 2008].

[29] All the range data for SELENE spacecraft are weighted at 5 m, and the Doppler data are weighted at 1 mm/s except for the data from the GN stations (2 mm/s) which have smaller dishes. The smaller observation sigmas for SELENE compared to those for the historical satellites (see section 3.2 or Table 2) are also chosen to emphasize the new SELENE tracking data in the solutions and to balance the discrepancy between the amount of data for the near and farside.

3.2. Processing of the Historical Tracking Data

[30] In addition to data from SELENE, historical tracking data from the Lunar Orbiters I-V, the Apollo 15 and 16 subsatellites, Clementine and Lunar Prospector were also included. For a good overview of data until Clementine, see *Konopliv et al.* [1993] and *Lemoine et al.* [1997], and for LP, see *Konopliv et al.* [2001]. Some SMART-1 tracking data, taken during January 2006 and a few days in May 2006, were included as well. Prior to SELENE, farside gravity information was obtained from the integrated effect of gravity on the satellite orbit, and decorrelation of signatures was greatly helped by the variety of near-equatorial inclinations of LO I-III and the Apollo 15 and 16 subsatellites [*Konopliv et al.*, 2001]. Even though SELENE has direct tracking over the farside, the varying orbit characteristics of the historical data mean that they sample the lunar gravity field in different ways, making them valuable for combination with SELENE data. On top of that, LP was tracked continuously and so it constitutes a tracking data set of high quality and high resolution, valuable for studying both the long- and short-wavelength signals.

[31] The data of LP are divided into two parts, depending on the mission phase as explained in section 1. For the processing of this study however, the extended mission data of LP were deliberately left out. At an average altitude of 30 km, they contain a lot of information about the gravity field at shorter wavelengths, but it was felt that combining these data together with farside data expected to be sensitive up to spherical harmonic degree 75 [*Matsumoto et al.*, 2008], would disrupt the gravity field too much, for example in terms of loss of correlation with topography, and the amount of trackiness in farside anomaly maps that can be seen in pre-SELENE models. Nevertheless, these data remain of high importance and will be included in future efforts, for example to focus on low lunar orbit determination (for which the LP extended mission data are indispensable).

[32] Average arc lengths for the historical data depend on the satellite and tracking characteristics. LO arcs were about half a day, with some longer ones included. The LO satellites were photographic precursor missions to the Apollo program, and because of this nature, there are a lot of pointing maneuvers occurring on the satellite, inducing spurious accelerations on the spacecraft. The times for these maneuvers are tabulated so they can be estimated, but they disrupt the data stream and severely limit the arc length. Furthermore, several arcs contained a large amount of these maneuvers, and those were left out of the processing. Apollo 15 and 16 subsatellites were free-flying satellites, but tracking of these satellites was sparse, so we were forced to process these data in short arcs from 2 hours to 1 day, with an average length of 8 hours. The Clementine data have an average arc length of 2 days, with several longer arcs of about 10 days included. The LP data were systematically processed in batches of 2 days. The SMART-1 data are also limited by maneuvers, and the rule for dividing the data into arcs was to avoid maneuvers not covered by tracking data, leading to an average of 15 hours for the January 2006 data. The May data were used as one 5-days arc. For LO and SMART-1, in the case of tabulated maneuvers, constant accelerations in three orthogonal directions during these maneuvers were estimated. Apollo 15 and 16 were free-flying satellites and thus without maneuvers. For LP and Clementine, the arc was simply split whenever a maneuver for altitude correction occurred. Similar to Rstar and Vstar, solar radiation pressure was modeled with a cannonball model for the historical satellites, and measurement biases on Doppler and range data are estimated, in particular for the case of LP, to absorb the signal induced on the Doppler data by the spin of the spacecraft as discussed before.

[33] All historical satellites except the Apollo subsatellites were tracked with the Deep Space Network (DSN) [*Lemoine et al.*, 1997; *Konopliv et al.*, 2001]. The Apollo subsatellites were tracked with the now no longer existing Manned Space Flight Network, and even though uncertainties remain in the coordinates of those sites, we used the same coordinates as previous analyses [*Lemoine et al.*, 1997; *Konopliv et al.*, 2001] and did not try to estimate them. The SMART-1 was tracked with the ESA network for which coordinates were provided (T. Morley, personal communication, 2006). For the LO data, DSN coordinates were mapped back to the respective epochs using International Earth Rotation Service site velocities, the same as was done before for the GLGM-2 model [*Lemoine et al.*, 1997]. The data weights are summarized in Table 2 together with those used for SELENE.

3.3. Gravity Estimation

[34] The lunar gravity potential, V, is modeled in spherical harmonics using the expansion,

$$V(\phi,\lambda,r) = \frac{GM}{r}\sum_{n=0}^{N_{\max}}\left(\frac{R}{r}\right)^n \sum_{m=0}^{n}\left(\overline{C}_{nm}\cos m\lambda + \overline{S}_{nm}\sin m\lambda\right) \cdot \overline{P}_{nm}(\sin\phi) \quad (2)$$

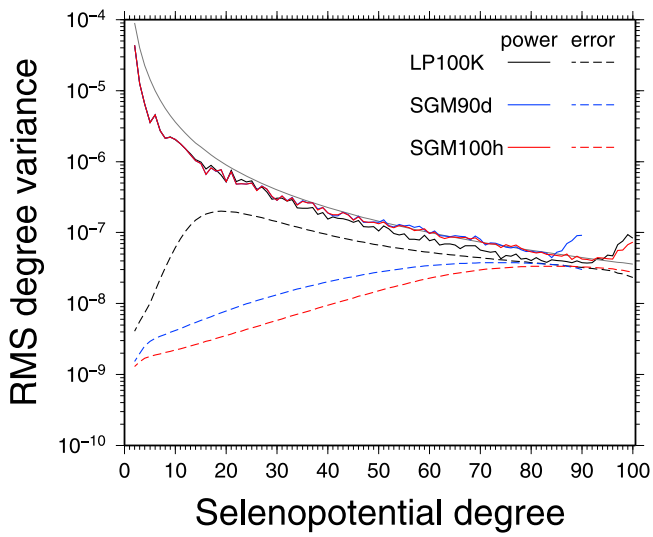

Figure 4. Comparison of RMS coefficient power and error degree variances for LP100K (black), SGM90d (blue), and SGM100h (red). The power and error are indicated by solid lines and broken lines, respectively. Indicated by gray solid line is the power law constraint of $\beta = 3.6$ which is applied to the models.

where the expansion is given in spherical coordinates with latitude ϕ, longitude λ, radius r, G is the universal constant of gravitation, M is the lunar mass, R is the reference radius of the Moon (1738.0 km for our models), $\overline{C}_{nm}$ and $\overline{S}_{nm}$ are the normalized selenopotential coefficients to be determined, and $\overline{P}_{nm}$ are the normalized associated Legendre functions of degree n and order m. The unnormalized coefficients are related to the normalized by

$$(C_{nm}; S_{nm}) = \left[\frac{(n-m)!(2n+1)(2-\delta_{0m})}{(n+m)!}\right]^{1/2} (\overline{C}_{nm}; \overline{S}_{nm}) \quad (3)$$

where δ_{0m} is Kronecker delta ($\delta_{0m} = 0$ for $m \neq 0$ and $\delta_{0m} = 1$ for $m = 0$). The harmonic coefficients of degree one are fixed to zero since the origin of the coordinate system is chosen to be the center of mass of the body. The maximum degree of expansion $N_{\max}$ is set to 100.

[35] The normal matrices were generated per setup. One setup generally involves one arc of one satellite, but those related to 4-way Doppler data are multisatellite setups in which Kaguya and Rstar are involved. They were then combined and inverted by the SOLVE program. Although the farside data gap is now filled with SELENE 4-way Doppler data of which coverage is shown in Figure 2, a Kaula type constraint of $\beta = 3.6$ was still applied. The constraint was introduced in order to suppress the excessive power of the coefficients of degree and order higher than 70, which results from the remaining small data gap in the northern farside. The solutions were globally iterated twice. The RMS differences in terms of free-air gravity anomaly (see equation 4) between the first and the second iterations was 17 mGal, and the solution has converged to this level. In addition to the gravity field up to degree and order 100, the lunar GM and the degree 2 potential Love number k_2 were also estimated.

4. Gravity Results and Comparison with Other Models

[36] The gravity solution derived by the above mentioned data processing is designated SGM100h. This section shows the gravity signature of the new model and compares SGM100h with one of the LP gravity models LP100K and/or SGM90d, one of the former SELENE gravity models, in terms of coefficient degree variances, gravity anomaly, projected error distribution, correlation with the topography, contribution of the observation to the solution, and orbit determination performance. Although LP100K is not the most recent LP gravity model, we choose this model for our comparison. This is because the LP models are mostly lumped-coefficient models which means that only full expansion gives the best integrated results [*Goossens and Matsumoto*, 2007], and LP100K has the same truncation degree as SGM100h.

4.1. Power of the Coefficients

[37] The RMS of coefficient power variance at degree n is represented as

$$\sigma_n = \left\{(2n+1)^{-1}\sum_{m=0}^{n}\left(\overline{C}_{nm}^2 + \overline{S}_{nm}^2\right)\right\}^{1/2} \quad (4)$$

and similarly replacing ($\overline{C}_{nm}$, $\overline{S}_{nm}$) with ($\sigma(\overline{C}_{nm})$, $\sigma(\overline{S}_{nm})$) gives the RMS coefficient error (or sigma) degree variance. Figure 4 shows the RMS coefficient power and error degree variances for LP100K, SGM90d, and SGM100h, together with the Kaula-type spectral power constraint used for these models. The SELENE models give the larger power variances beyond degree 35 compared to LP100K, and the maximum deviation of SGM100h with respect to LP100K is

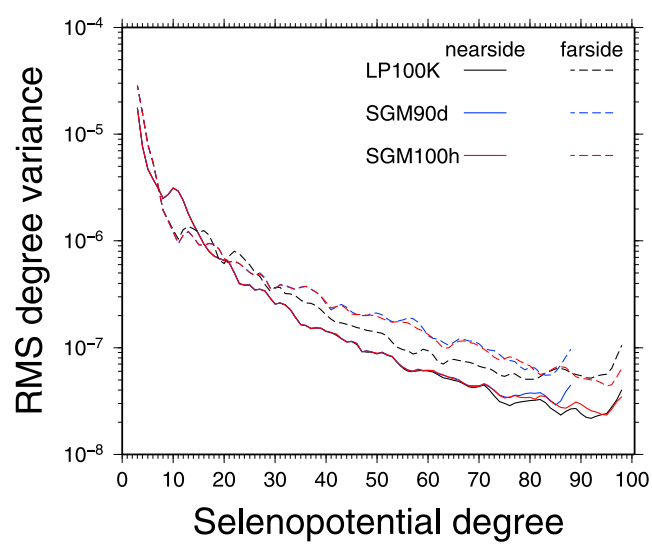

Figure 5. RMS coefficient power degree variances which are localized on the nearside (solid lines) and the farside (broken lines) for LP100K (black), SGM90d (blue), and SGM100h (red).

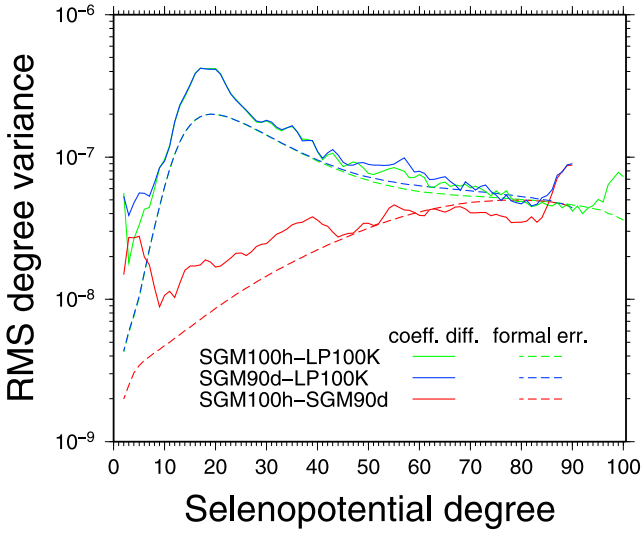

Figure 6. RMS degree variances of coefficient differences between two models (solid lines) and those of formal errors (broken lines). Results are shown between SGM100h and LP100K (green), between SGM90d and LP100K (blue), and between SGM100h and SGM90d (red). The formal errors are calculated as the sum of two models compared.

observed at degree 56 where the former has a factor of 1.46 larger RMS variance. The larger global power for SELENE models is due to the increased power in the farside. This is confirmed by looking at the RMS power variances computed from coefficients which are localized on the nearside and the farside (Figure 5). The nearside powers of the three models are almost identical below degree 70, while in the farside, the SELENE models have factors of 1.3 to 2.1 larger RMS variances with respect to LP100K for degrees 35 to 80. This indicates that the SELENE models more realistically resolve the gravity in the farside that has rougher topography than nearside, which will be further discussed in section 4.3 by computing the correlation between gravity and topography. The ratio of the farside RMS variances with respect to those of the nearside that are averaged over degree beyond 35 is 2.1 for SGM100h. The lunar dichotomy is clearly visible in terms of the coefficient power. The power variances have a hump near the maximum expansion degree, which is probably due to the spectral leakage effect from the unmodeled higher-degree terms. The magnitude of the hump is larger for LP100K compared to SGM100h, because LP100K includes the data from the low-altitude extended mission of LP, having more sensitivity to the high-degree terms, while SGM100h only includes the data from LP nominal mission.

[38] The RMS coefficient error variances (see Figure 4) for LP100K have a convex shape with its peak at n = 19 beyond which the error curve follows the a priori power law. Pre-SELENE spherical harmonic gravity models have similar error spectra, and the investigation of features such as nearside and farside crustal dichotomy is limited to the peak degree [*Konopliv et al.*, 2001]. However, owing to the farside tracking data, the degree-wise errors are significantly reduced for SELENE models with their peaks at n = 74 for SGM90d and n = 84 for SGM100h. The larger amount of SELENE tracking data included in SGM100h leads to the totally smaller formal error compared to SGM90d. The maximum improvement of SGM100h over LP100K is observed at n = 17 with a factor of 63, and the lowest degree coefficients are improved by a factor of 3.1 (in terms of "formal" error; see discussion in the next paragraph). Although the farside tracking data to some extent contribute to reduce the errors in low-degree coefficients, the contribution from LP data is still large since the mean arc lengths of Rstar and Vstar, for which the data densities are sparse, are shorter than 3 days. The low-degree coefficients will be further improved by realizing longer arc lengths of the subsatellites with differential VLBI data which will complement the Doppler and range data in both quality and quantity, or by extending LP arcs.

[39] The formal errors in Figure 4 can be to some extent verified by comparing them with the differences in the coefficients between two models. We compared three combinations of the differences between LP100K, SGM90d, and SGM100h in terms of the RMS degree variances (see Figure 6). Note that the RMS error variances are not identical with those in Figure 4, but expressed as the sum of two models compared, i.e., $\sigma_{n,1+2} = \{(2n+1)^{-1}\Sigma_{m=0}^{n}[\sigma(\overline{C}_{1nm})^2 + \sigma(\overline{S}_{1nm})^2 + \sigma(\overline{C}_{2nm})^2 + \sigma(\overline{S}_{2nm})^2]\}^{1/2}$ with the subscripts 1 and 2 denoting each model. For all the comparisons, the coefficient differences agree with the formal errors within a range of 3 sigmas for $n \geq 8$, indicating slightly optimistic data weights used for these models. However, there are larger deviations for the lower-degree terms. In particular, discrepancies exceeding 10 sigmas occur at degree 2 for the comparisons of SGM100h-LP100K and SGM90d-LP100K, and at degree 3 for the comparison of SGM100h-SGM90d. One of the reasons for the large low-degree coefficient

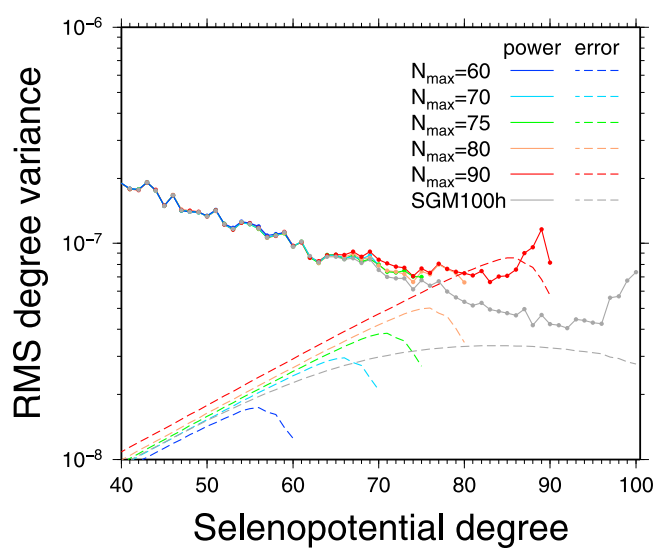

Figure 7. RMS coefficient power and error degree variances for unconstrained solutions expanded up to degree and order 60 (blue), 70 (light blue), 75 (green), 80 (orange), and 90 (red). The degree variances for $n \geq 40$ are shown. The power and error variances are indicated as solid lines and broken lines, respectively. The gray lines are the RMS degree variances for SGM100h (a constrained solution) for comparison.

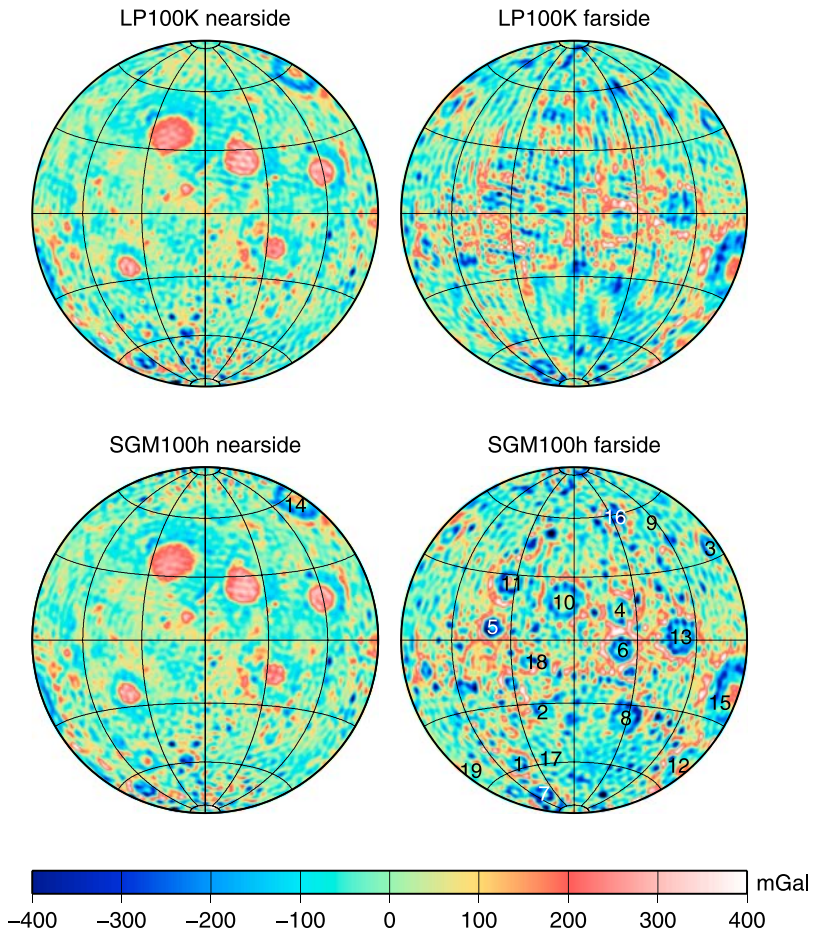

Figure 8. Free-air gravity anomalies at the lunar surface for (top) LP100K and (bottom) SGM100h, computed with respect to a reference radius of 1738.0 km. The nearside maps are on the left and the farside on the right. Unit is in mGal. The anomalies are evaluated up to degree and order 100. The numbers on the figure indicate the locations of the basins tabulated in Table 3.

differences which appear even in the comparison between two SELENE models may be due to the different arc length of Rstar, i.e., 12 hours for SGM90d and 2.6 days for SGM100h. The absolute error of a particular model cannot be distinguished by such comparisons, but we believe that SGM100h has the smallest error. Nevertheless, one still needs to be careful with any geophysical interpretation of the lowest degree coefficients until the differential VLBI data are incorporated and longer arc lengths are realized for Rstar, Vstar, and also for LP, by which more stable determination of the low-degree coefficients can be expected.

[40] We investigated to what degree and order unconstrained solutions can be realistically derived from the current data set. Figure 7 shows the degree variances for the unconstrained solutions expanded up to degree and order 60, 70, 75, 80, and 90. The coefficient power variances of the unconstrained solutions below degree 70 are almost identical with that of SGM100h (a constrained solution with $\beta = 3.6$). This means that the selected β value is reasonable and does not unnecessarily suppress the coefficient power. Provided that the signal power of SGM100h is realistic, the signal to noise ratios for the unconstrained solutions of $n \leq 80$ are larger than one, but the unconstrained power starts to deviate from the constrained solution near degree 70 which is considered to be the limit for the best determined gravity field based on the current data set. Further discussions on the information content will be made in sections 4.3 and 4.4.

4.2. Gravity Anomalies and Selenoid

[41] Figure 8 shows the free-air gravity anomalies from LP100K and SGM100h which are computed with respect to a reference sphere with radius of 1738.0 km, and with full expansion degree and order up to 100. Here, the free-air gravity anomaly, FA, is defined as

$$FA(\phi, \lambda, r) = \frac{\partial V}{\partial r} - \frac{2V}{r} = \frac{GM}{r^2} \sum_{n=0}^{N_{\max}} (n-1) \left(\frac{R}{r}\right)^n \cdot \sum_{m=0}^{n} \left(\overline{C}_{nm} \cos m\lambda + \overline{S}_{nm} \sin m\lambda\right) \overline{P}_{nm}(\sin \phi) \quad (5)$$

The color scale of Figure 8 is truncated at ±400 mGal, but the maximum and minimum anomalies of SGM100h are 695 and −730 mGal located at (32° E, 85° S) and (273° E, 80° S), respectively. There are only small differences in the nearside between the two models, since it is well covered by the conventional 2-way observables. In the farside,

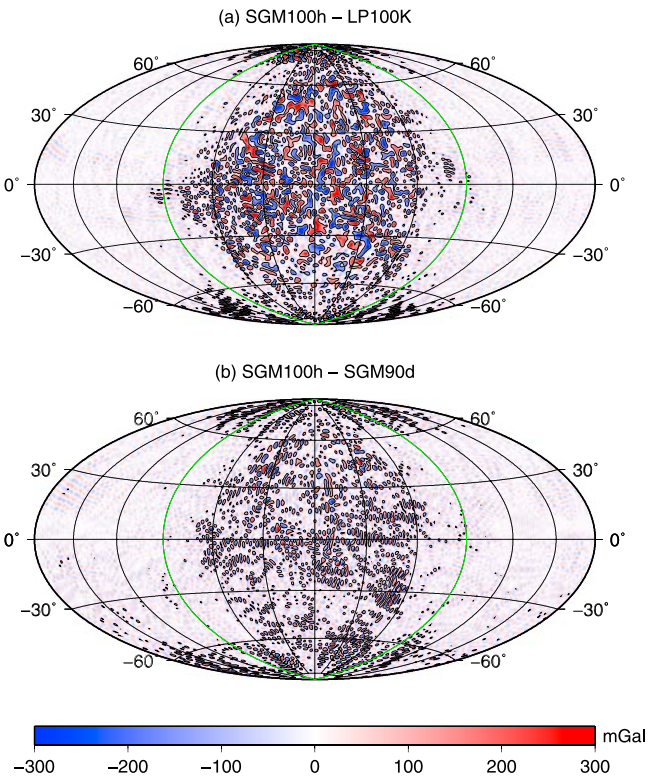

Figure 9. Maps showing free-air gravity anomaly differences between (a) SGM100h and LP100K, and (b) SGM100h and SGM90d. Unit is in mGal. The maps are centered on 180°E longitude. Contour lines are drawn at −100 and 100 mGal. Green lines indicate the boundary between the nearside and the farside.

however, noticeable differences can be observed. Despite the lack of direct farside tracking data, it is remarkable that the gravity signatures of major impact basins such as Coulomb-Sarton, Moscoviense, Freundlich-Sharanov, Dirichlet-Jackson, Hertzsprung and Korolev are partly visible in LP100K. However, they are only partially resolved and require information from all the historical data to be seen [*Konopliv et al.*, 2001]. On the other hand, the ringed gravity signatures of the above mentioned six basins as well as Mendeleev, Apollo and Planck, corresponding to the topographic structures, are more clearly visible in SGM100h. Moreover, many large craters with sizes of one or two hundred kilometers can be identified as a negative gravity anomaly in SGM100h.

[42] The free-air gravity anomaly differences between SGM100h and LP100K and those between SGM100h and SGM90d are shown in Figures 9a and 9b, respectively. For both the comparisons, the large differences exceeding ±100 mGal are confined in the farside and poleward of 60°. The farside region with the large differences extends from 120° E to 240° E, corresponding to the data gap that existed before SELENE. The range of the differences in Figure 9a is from −493 to 548 mGal, and that in Figure 9b is from −345 to 343 mGal. The RMS differences of SGM100h with respect to LP100K are 78 mGal (global), 48 mGal (nearside) and 99 mGal (farside), and those with respect to SGM90d are 62 mGal (global), 49 mGal (nearside) and 73 mGal (farside). The differences between SGM100h and SGM90d arise partly from the difference in the maximum expansion degree, however judging from the larger differences in the farside, the newly added 4-way Doppler data in SGM100h are considered to contribute to the refinement of the farside gravity. The differences in the polar regions both in the nearside and farside seen in Figure 9a may be partly due to the difference in the way of weighting the LP tracking data; *Konopliv et al.* [2001] downweighted with the factor of $\cos^{-1/2}\phi$ where ϕ being the latitude, while our analysis did not adopt the downweighting. It is suggested that our models are more realistic by seeing localized correlations with topography (see section 4.3).

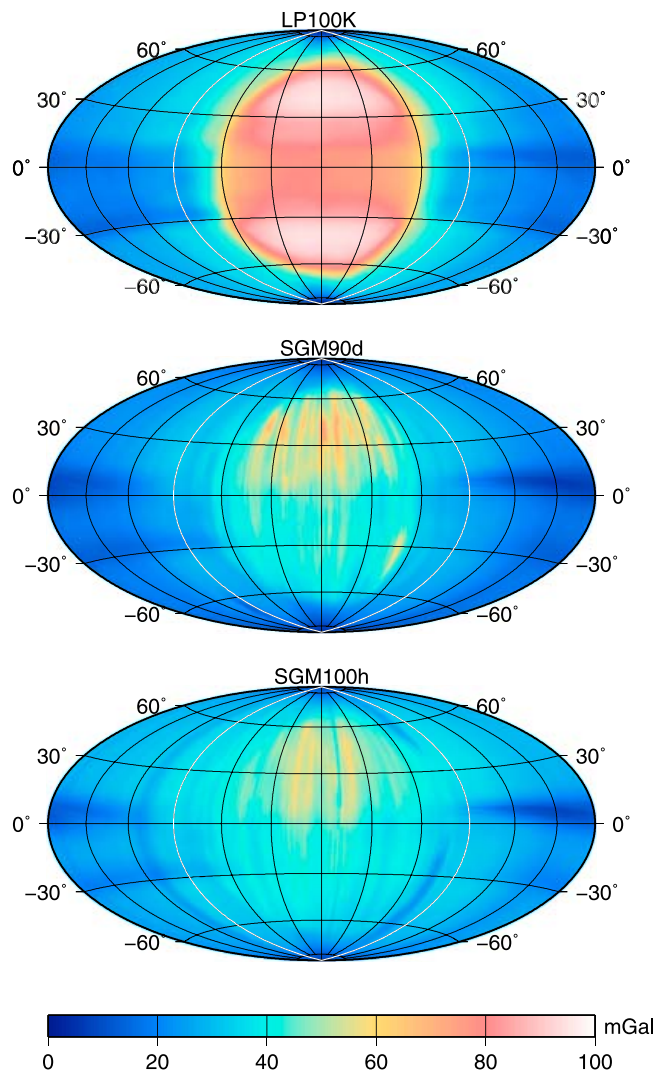

Figure 10. Projected errors of free-air gravity anomaly for (top) LP100K, (middle) SGM90d and (bottom) SGM100h which are calculated from the full covariance matrices up to degree and order 90 for SGM90d and 100 for LP100K and SGM100h. Unit is in mGal. The maps are centered on 180°E longitude. White lines indicate the boundary between the nearside and the farside.

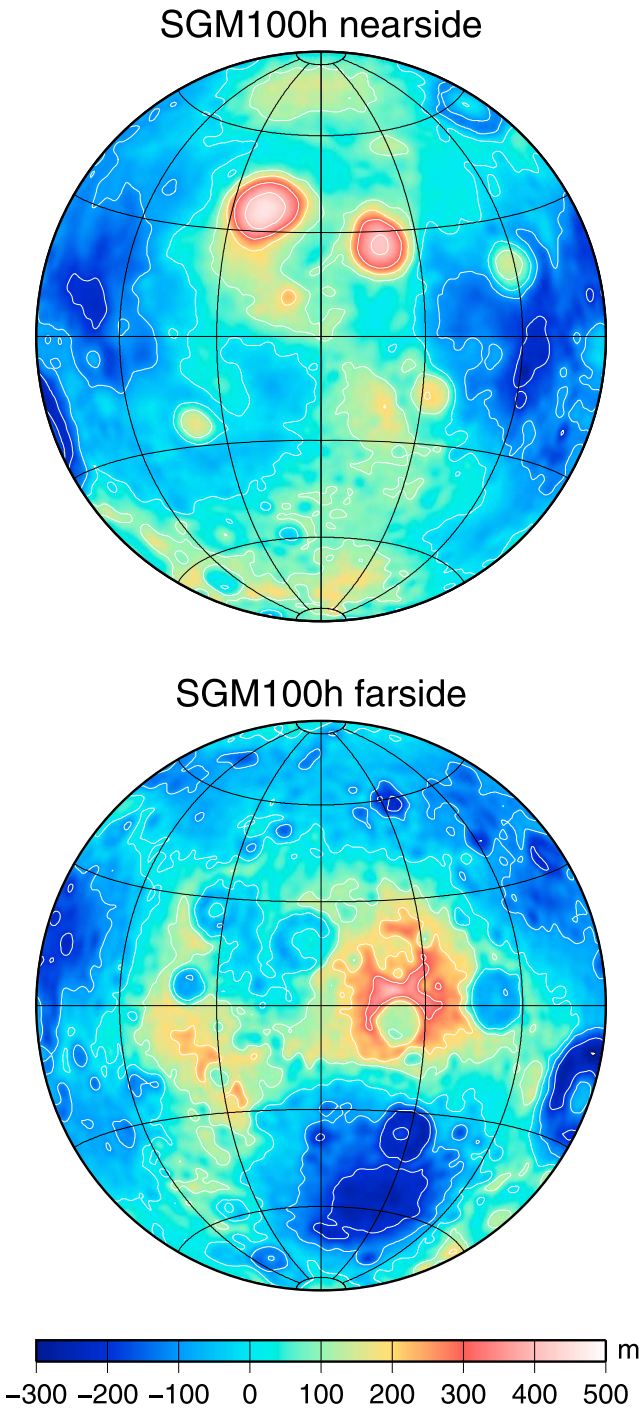

Figure 11. Selenoid (lunar geoid) with respect to 1738 km reference sphere which is calculated from SGM100h model with J_2 term excluded. Unit is in meter. Contour interval is 100 m.

[43] Depicted in Figure 10 are the projected errors of the free-air gravity anomalies for LP100K, SGM90d and SGM100h, which are calculated from the full covariance matrices. Once again the large errors are seen in the farside data gap region for LP100K, but they are significantly reduced in the SELENE models. The projected errors for LP100K range up to 95 mGal, while the maximum errors for SGM90d and SGM100h are 75 mGal and 62 mGal, respectively. The bifurcation of the errors for LP100K (smaller uncertainties in the lower latitudes) is due to the contribution from tracking data of LO I-III and Apollo 15/16 subsatellites with inclinations between 0° and 30° [*Konopliv et al.*, 2001], and similar reduction of the errors (but only in the nearside) in the latitudinal range are also seen in the SELENE models. The errors averaged over the nearside and the farside are 25 and 55 mGal for LP100K, 20 and 33 mGal for SGM90d, and 26 and 35 mGal for SGM100h, respectively. Although the smallest mean errors are seemingly given by SGM90d, it is due to its lower truncation degree at 90. The slightly larger nearside error of SGM100h compared to LP100K is likely due to the fact that SGM100h does not contain the low-altitude LP extended mission data which have more sensitivity to high-frequency gravity field. The similar (but in a reverse sense) consideration concerning satellite altitude can be applied to the smaller farside error for SGM100h along the longitude of about 190° E, which seems to be related to the Kaguya's lower orbit with altitude of about 60 km corresponding to the 4-way pass on 30 January 2009. Even with SGM100h, there still is an unbalanced error distribution in the farside, with larger uncertainties in the northern hemisphere, corresponding to the smaller 4-way Doppler data density in that region (see Figure 2). Nevertheless, what is emphasized here is that SGM100h shows the most homogeneous error distribution over the Moon among the three models compared.

[44] Figure 11 shows the selenoid (the lunar geoid) from SGM100h with J_2 term removed. The total range in the selenoid is from −302 to 463 m (−533 to 569 m with J_2 term) which is almost same as that of LP100K. Since the geoid is essentially an integration of the gravity anomalies, it attenuates the high-frequency parts of the gravity. The overall feature thus remains unchanged from previous models, showing the selenoid highs at the nearside principal mascons as well as near the farside highlands, selenoid lows in the South Pole-Aitken basin (SPA), and the moats in the Orientale basin, etc. However, SGM100h exhibits greater detail in the farside selenoid for the major impact basins as well as large craters, with their ringed shapes clearly resolved. The differences of the selenoid between SGM100h and LP100K (not shown) range from −127 m to 155 m, with large differences again confined in the longitudinal zone from 120° E to 240° E. The RMS differences between the two models are 3.7 m and 22.9 m for the nearside and the farside, respectively.

[45] Depicted in Figure 12 are Bouguer gravity anomalies computed from SGM100h and a topographic model from SELENE laser altimeter (LALT), i.e., STM-359_grid-03 (an updated version of *Araki et al.* [2009]) which is based on the altimetric observations during the nominal mission period. A crustal density of 2800 kg/m^3 is assumed and no correction for mare basalt is applied. The high-frequency "spotty" signatures are likely due to the less accurate gravity coefficients above degree 70 (see discussions in sections 4.1, 4.3 and 4.4), and disappear when the coefficients are truncated at this degree. The Bouguer anomalies are characterized by strong positive plateaus at nearside principal mascons, and for the basins in the farside and limb, by the gravity highs at the basin center relative to the surrounding floor. The farside concentric structures seen in the free-air gravity anomaly map (Figure 8) almost disappear in the

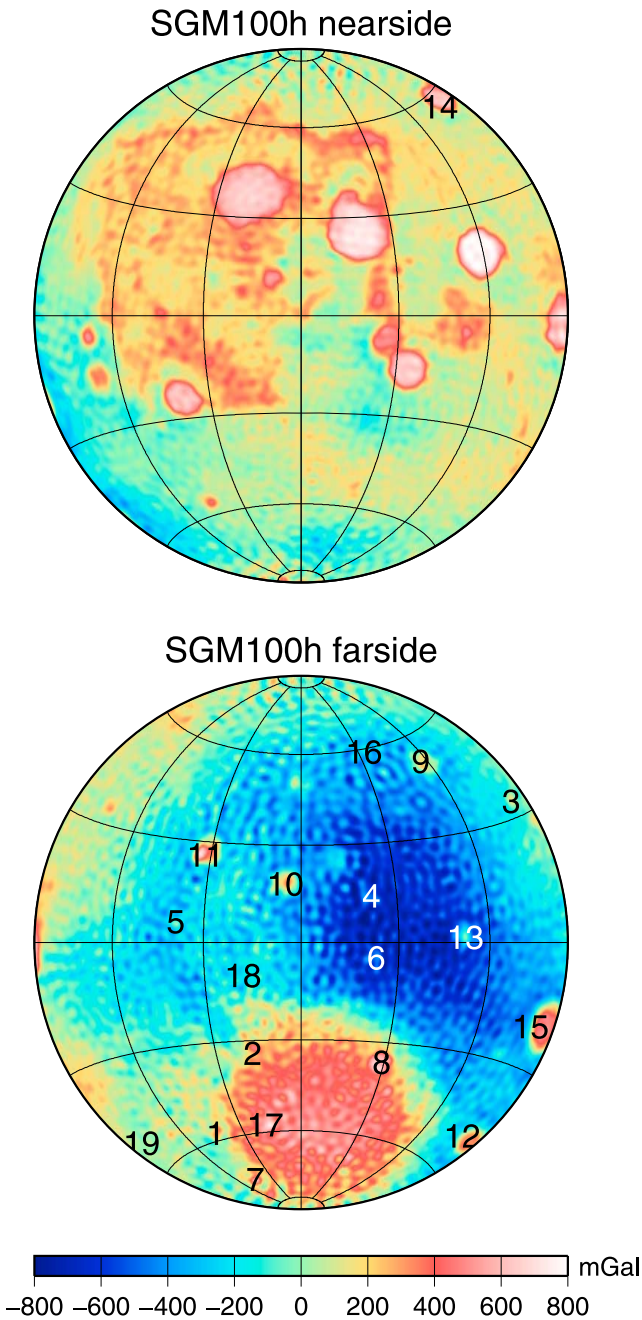

Figure 12. Bouguer gravity anomalies evaluated at lunar surface with reference radius of 1738 km, which is calculated from SGM100h gravity model and STM-359_grid-03 topographic model by SELENE laser altimeter (an updated version of *Araki et al.* [2009]). Unit is in mGal. The coefficients up to degree and order 100 are included, and a crustal density of 2800 kg/m^3 is assumed. The numbers on the figure indicate the locations of the basins tabulated in Table 3.

Bouguer anomaly map (Figure 12), leaving the relative gravity highs only at the basin center, which suggests the existence of excess mass below the center.

[46] *Namiki et al.* [2009] examined the peak heights of the free-air and Bouguer anomalies for major impact basins and classified them into three categories, i.e., principal mascons, Type I and II basins [see *Namiki et al.*, 2009, Table 1]. The Type I basins have similar peak heights for both the free-air and Bouguer anomalies, whereas the Type II basins have smaller peak magnitudes in the free-air anomalies (40–80% compared to those in the Bouguer anomalies) and broader peak shapes. We reexamined, by using SGM100h, their classification for the major impact basins in the farside and limb regions, and the results are summarized in Table 3. Table 3 contains the gravity values at the floor and the center of the basins which were read out from the north-south profiles of the free-air and Bouguer anomalies. The gravity values at the floor are calculated as the average of those at the northern and southern floors. The classification of *Namiki et al.* [2009] is unchanged here, but four basins which were reported as "unclassified" or not listed by *Namiki et al.* [2009] are now classified; Dirichlet-Jackson, Ingenii, and Schrodinger are Type I, and Coulomb-Sarton is Type II. We also investigated two other large basins, the Australe and Keeler-Heaviside basins, and found that they do not show distinct central peaks either in the free-air or Bouguer anomalies. We propose a new class for these basins, i.e., "nonmascon basins" to distinguish them from others by the lack of obvious gravity anomalies. The Poincare basin does have a central peak, but its gravity signature is different from those of other basins in the SPA such as Apollo, Ingenii, Planck, and Schrodinger, i.e., the profile is smoother, the peak magnitude is smaller, and the ring structures in the free-air anomaly are indistinct. The Birkoff basin is also characterized by a weak peak magnitude. We thus labeled Poincare and Birkoff as nonmascon basins.

[47] In the farside hemisphere, the gravity field around the SPA is best determined because of the densest 4-way Doppler data coverage in this region. The SPA is characterized by the nearly zero free-air gravity anomalies and strong positive Bouguer gravity anomalies, which suggest the state of isostasy and the thin crust in this region. *Garrick-Bethell and Zuber* [2009] recently identified an elliptical signature of the SPA by fitting ellipses to the topography from the Clementine, and the LP-derived iron and thorium signatures. It is interesting to conduct an additional test in terms of gravity signature. When cross-section profiles of the free-air gravity anomaly and the topography are plotted along a line that passes through the center of the SPA, one sees oscillations in the free-air anomalies corresponding to the small-scale topographic variations, but the profile is rather flat around zero. On the other hand, when a Bouguer anomaly profile is similarly plotted, it exhibits rises, from which the elliptical signature can be identified, i.e., by comparing two profiles which are orthogonal to each other, with one representing the semi-major axis a and the other the semiminor axis b. With a single profile, however, it is sometimes difficult to detect the rising points which are obscured by local high-frequency oscillations. In order to suppress the local high-frequency oscillations and to make the analysis more reliable, the profiles of the two gravity anomalies and the topography were first calculated with an 1 degree step of tilt angle (or orientation), and the profiles with specific tilt angles were then calculated by averaging 21 profiles within ±10 degrees from the tilt angle of interest. The gravity anomalies were calculated by truncating degree and order at 70. We examined several sets of the profiles by changing the orientation

Table 3. Classifications of Major Impact Basins on the Farside and Limb Regions[a]

Basin Number and Name[b]	Basin Center[c] Lon (° E)	Basin Center[c] Lat (° N)	Diam[d] (km)	FA flr	FA cnt	BA flr	BA cnt	FA Height	BA Height	Age[e]	Type[f]
1 Planck	135.5	−57.5	325	−210	80	0	310	290	310	PN	I
2 Ingenii	163	−34	325	−200	100	160	450	300	290	PN	I
3 Lorentz	263	34	365	−200	60	−150	170	260	320	PN	I
4 Dirichlet-Jackson	202	14	470	−250	60	−760	−480	310	280	PN	I
5 Mendeleev	141	6	365	−440	−30	−360	0	410	360	N	I
6 Korolev	203	−4.5	440	−270	0	−710	−420	270	290	N	I
7 Schrodinger	134	−75	320	−350	120	70	650	470	580	I	I
8 Apollo	209	−36	480	−310	60	190	670	370	480	PN	II
9 Coulomb-Sarton	237	52	530	−170	40	−350	190	210	540	PN	II
10 Freundlich-Sharanov	175	18	600	−250	80	−440	300	330	740	PN	II
11 Moscovience	148	26	420	−300	150	−260	540	450	800	N	II
12 Mendel-Rydberg	266	−50	420	−110	180	−370	390	290	760	N	II
13 Hertzsprung	231.5	1.5	570	−250	190	−670	0	440	670	N	II
14 Humboldtianum	84	61	700	−290	150	−10	660	440	670	N	II
15 Orientale	265	−20	930	−310	250	−410	500	560	910	I	II
16 Birkoff	213	59	330	−320	−120	−350	−220	200	130	PN	NM
17 Poincare	162	−57.5	340	−160	30	360	610	190	250	PN	NM
18 Keeler-Heaviside	162	−10	780	No central peak	No central peak	No central peak	No central peak	No central peak	No central peak	PN	NM
19 Australe	94.5	−51.5	880	No central peak	No central peak	No central peak	No central peak	No central peak	No central peak	PN	NM

[a]The gravity anomalies are in mGal. Lon, Longitude; Lat, Latitude; Diam, Diameter; FA, Free-air anomaly; BA, Bouguer anomaly; flr, floor; cnt, center.
[b]The basin numbers are plotted in Figures 8 and 12 to locate the basins.
[c]*Wilhelms et al.* [1987].
[d]Major topographic rim among multirings [*Wilhelms et al.*, 1987].
[e]PN, N, and I indicate Pre-Nectarian, Nectarian, and Imbrian, respectively.
[f]I, II, and NM indicate Type I, Type II, and nonmascon basins, respectively.

of the profiles with a 10° step, and with the basin center assumed to be located at (191°.1 E, 53°.2 S) [*Garrick-Bethell and Zuber*, 2009]. An orientation angle of -10° gave the most enhanced elliptical signature (or the highest a/b ratio) and the results with this angle are plotted in Figure 13. The axes measure about 2800 by 2000 km and the a/b ratio is 1.4. When the profiles are further rotated by 45°, the length of both the axes become almost identical being about 2300 km. According to the outer topography results of *Garrick-Bethell and Zuber* [2009], the size is 2400 by 2050 km, the a/b ratio is 1.17, and the tilt angle is −18°.8. Our result gives the tilt angle which is close to their value, but suggests a more elliptical shape. Judging from the fact that points C and D are at almost the same distance from the assumed basin center (Figure 13c), the center suggested by *Garrick-Bethell and Zuber* [2009] seems more reasonable than that by *Wilhelms et al.* [1987] (the black dot in Figure 13a, (180° E, 56°.5 S)), but the center might be shifted poleward (Figure 13b). Although our analysis is rather simple, an elliptical signature of the SPA, that suggests an oblique impact, has been confirmed by two orthogonal profiles of the Bouguer gravity anomalies with tilt angles of −10° and −100°. More detailed elliptical parameters in gravity (i.e., a, b, center coordinates, and an orientation angle) can be investigated by fitting an ellipse to the Bouguer gravity anomaly signature.

4.3. Correlation With Topography

[48] Correlations between gravity and topography can give insight into the planet's state of compensation [*Watts*, 2001]. For the terrestrial planets, the higher-degree gravity signals are thought to mostly come from uncompensated topography, and in general, higher correlation values between topography and gravity are judged to be indications of better models [e.g., *Konopliv and Sjogren*, 1994; *Lemoine et al.*, 2001; *Han et al.*, 2009]. Here, the gravity models are evaluated by computing the correlation with the lunar topography as determined by LALT. The global correlations computed from the spherical harmonic coefficients of LP100K, LP150Q, SGM90d, and SGM100h fields with coefficients from LALT data are illustrated in Figure 14. The negative correlations at degrees 10 and 20 for LP100K and LP150Q are previously attributed to the nearside principal mascons, but one at degree 20 is found to be due to the farside uncertainties of the pre-SELENE models [*Namiki et al.*, 2009]. For high degree terms, the LP models hit the peak of about 0.7, while SELENE models give the correlations as high as about 0.9. Considering the fact that there are no essential differences in the nearside gravity coefficient powers (Figure 5), the increased correlations observed for SELENE models are due to the better determined farside gravity field. The correlations that are localized poleward of 60° are calculated (not shown), which shows larger correlations for SELENE models than for LP100K, indicating that 4-way Doppler data also contribute to better determination of polar gravity field.

[49] SGM100h generally shows the highest correlations below degree 90, but there is a dropoff of the signal after degree 70, which indicates the resolution limit of the modeled farside gravity field, since the topography model has much finer spatial resolution. The dropoff for SGM100h beyond degree 90 is sharp, showing even lower correlations than those for LP150Q which gives relatively flat signals from degree 50 to 100. This indicates that SGM100h loses

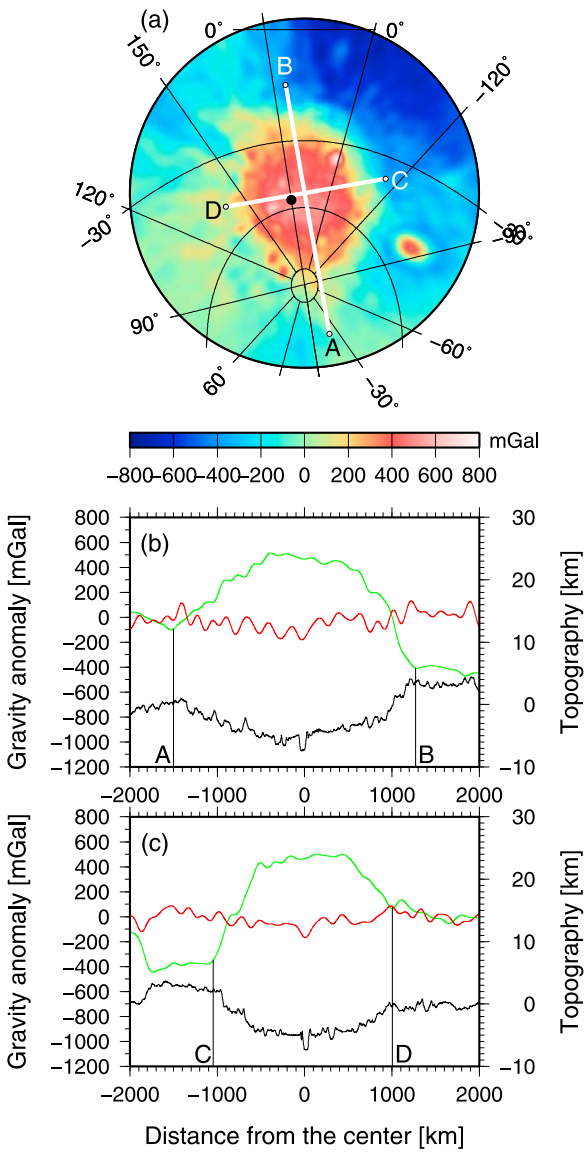

Figure 13. (a) A Bouguer anomaly near the South Pole-Aitken basin with the gnomonic map projection centered at (191°.1 E, 53°.2 S) [*Garrick-Bethell and Zuber*, 2009]. Black dot indicates the basin center suggested by *Wilhelms et al.* [1987]. (b) Cross-section profiles of the free-air gravity anomaly (red), the Bouguer gravity anomaly (green), and the topography (black) along the line A–B that is indicated in Figure 13a. The values of the gravity and topography are from SGM100h up to degree and order 70 and STM-359_grid-03, respectively. The points A and B correspond to the rising corners of the Bouguer anomalies. The profiles are shown by extending them beyond the two points to make the rising corners visible. (c) Same as Figure 13b, but along the line C–D.

the sensitivity even in the nearside due to the lack of LP extended mission data.

[50] Figure 15 compares the correlations for unconstrained solutions expanded up to degree and order 60, 70, 75, 80, and 90. The correlations are near 0.9 for $50 < n < 70$, but for $Nmax \geq 75$ solutions, dropoffs are observed after

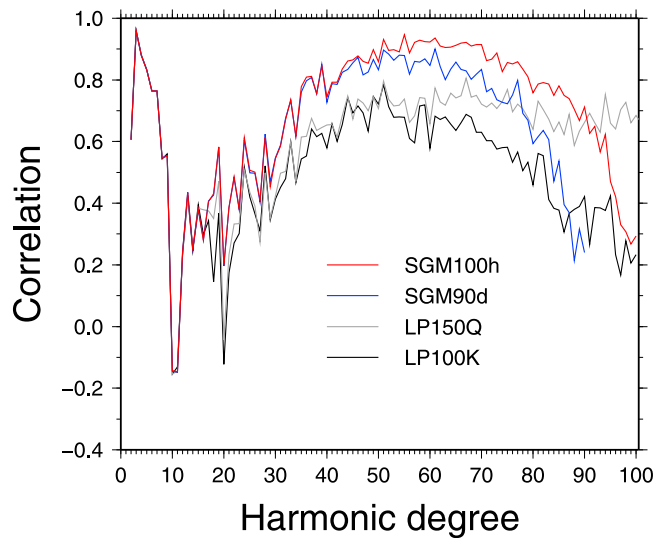

Figure 14. Global correlations between gravity and topography. The STM359_grid-03 model from SELENE laser altimeter is used for the lunar topographic model. The correlations are displayed for SGM100h (red), SGM90d (blue), LP100K (black), and LP150Q (gray).

degree 70 which are much sharper than that of constrained solution. Thus the same indication as derived from Figure 7 holds here, i.e., the gravity data set of this study has global sensitivities up to degree 70.

4.4. Gravity Assessment Via Contribution Measure

[51] The gravity models can also be assessed by calculating contribution measure. The idea is that if the underlying observational models are correct, the unknowns are in

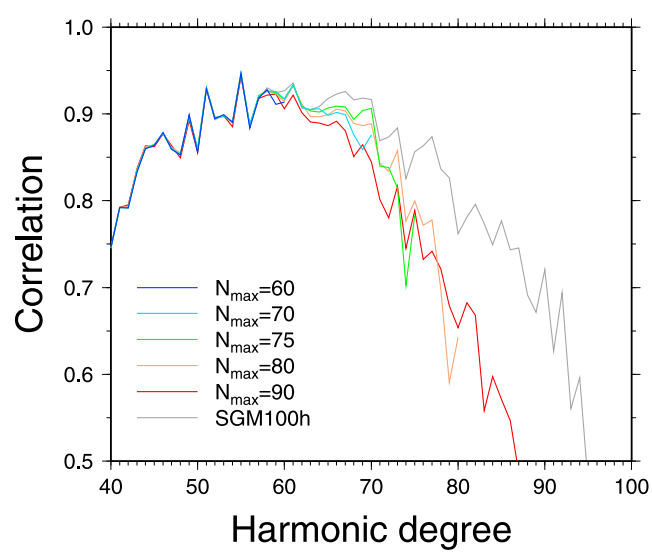

Figure 15. Same as Figure 14, but for unconstrained solutions expanded up to degree and order 60 (blue), 70 (light blue), 75 (green), 80 (orange), and 90 (red). The correlations for $n \geq 40$ are shown. The gray line is the correlations for SGM100h (a constrained solution) for comparison.

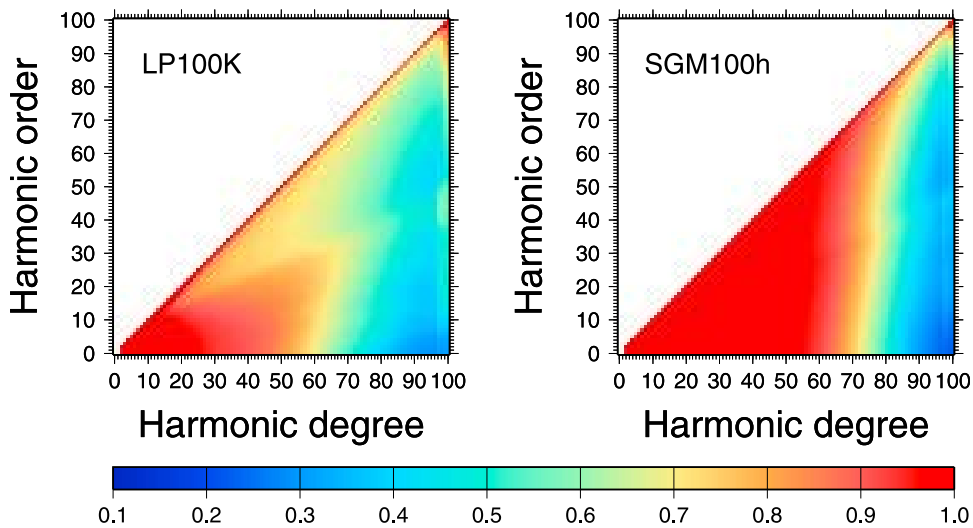

Figure 16. Contribution of the observations to the retrieved gravity field coefficients for (left) LP100K and (right) SGM100h. The value of one means that the coefficient is completely determined by the observations, while zero means that there is no contribution from the observation and the coefficient is completely determined by the a priori information.

part determined by the observations and in part by the a priori information (see Chapter 4.4.2 of *Floberghagen* [2002]). The contribution of the observations to the solution of the unknowns is given as

$$\mathbf{B} = \left(\mathbf{A}^T\mathbf{P}^{-1}\mathbf{A} + \mathbf{Q}^{-1}\right)^{-1}\mathbf{A}^T\mathbf{P}^{-1}\mathbf{A} \tag{6}$$

where **A** is design matrix, **P** is a priori covariance matrix for the data and **Q** is that for the model (i.e., the Kaula rule), respectively. The diagonal elements of **B** give the contribution measure ranging from 0 to 1, where an unit value implies that the observations completely determine that specific unknowns.

[52] Figure 16 shows the contribution measures for LP100K and SGM100h in which only $\overline{C}_{nm}$ coefficients are plotted, since the situation for $\overline{S}_{nm}$ coefficients is nearly identical. With the exception of the near sectorial ($n = m$) terms, coefficients up to degree ~55 and order ~20 have an observation contribution larger than 80% for LP100K. On the other hand, many more coefficients are better determined by the observations for SGM100h where the coefficients up to degree and order ~70 are determined with observational contribution factor larger than 80%, which is owing to the 4-way Doppler data (see also the simulation results of *Matsumoto et al.* [2008]). For coefficients with degree higher than 80, however, LP100K generally outperforms SGM100h which is again due to the inclusion of the LP extended mission data in LP100K and not in SGM100h.

4.5. Postfit Residual and Orbit Determination Performance

[53] One other way of comparing gravity field models is by assessing their performance in terms of orbit determination precision. There are several ways that this can be done. One way is to look at post-fit data residuals. In supporting online materials *Namiki et al.* [2009] showed that SGM90d produced data fit levels similar to LP100K, evaluated for tracking data of Lunar Prospector in July 1998, during its nominal mission. Due to its higher expansion and the inclusion of more tracking data, SGM100h performs slightly better than SGM90d, and in general slightly better than LP100K as well, for these same test data. All models have a data fit level of about 0.5 mm/s for these data.

[54] The RMS of postfit residuals for all the data that went into SGM100h can be seen in Table 2. Most of the postfit residuals are below the chosen values of data weight (or observation sigma), indicating that the data sigma are not optimistically too small. For those satellites with postfit residuals close to or even beyond their data weight (LO-I and A16, and LO-IV, respectively), it should be noted that the data weights listed in Table 2 are the average data weights. Some arcs show outliers in terms of data fit, and those are downweighted such that their data weight value is always larger than the postfit RMS. The 4-way Doppler residual values (0.48 mm/s RMS) are almost uniformly distributed over the farside and the limb regions (Figure 2), which implies that the gravity information in the observable is successfully extracted.

[55] Orbit overlap analysis is another powerful tool when comparing gravity model performance in orbit determination. In orbit overlap analysis, two arcs are constructed in such a way that there is an overlapping part between them. Orbit differences between the two determined orbits during the overlapping parts can then be computed, and they indicate the consistency between the two orbit solutions. As such, the overlaps are a measure of both the gravity field performance, and the chosen orbit determination parametrization.

[56] Overlaps were computed using LP data in July 1998. The arcs were chosen to be 2 days long, the same as in the gravity field data processing, and the overlaps were chosen to be 1 day, so as to have many orbital revolutions included in the orbit comparisons. The estimated parameters con-

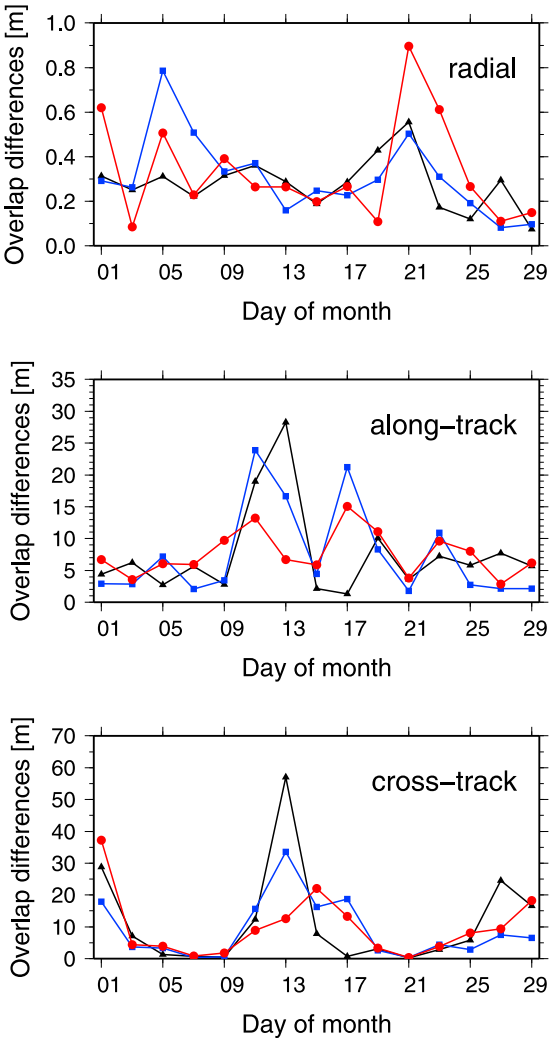

Figure 17. RMS of orbital overlap differences in (top) radial, (middle) along-track, and (bottom) cross-track directions. The orbital differences are computed for Lunar Prospector 2 day arcs during July 1998, with 1 day overlaps. Results with three gravity field models are shown for LP100K (black triangles), SGM90d (blue squares), and SGM100h (red circles).

sisted of the initial state vector, a solar radiation pressure coefficient, and measurement biases per pass per station. The RMS of orbital differences in radial, along-track (the transverse direction along the velocity vector) and cross-track (the normal to the other two directions) are shown in Figure 17. All models show differences at the same level, though for all comparisons, one should keep in mind that LP100K also includes the extended mission data of LP, whereas the SELENE models don't. For the radial direction, LP100K produces slightly more consistent results, but it should be noted that the outlier in the Figure for SGM100h constitutes an RMS difference of about 40 cm. All models show a radial consistency of less than 1 m, with an average of 50 cm, for the tested polar orbit at 100 km altitude.

[57] As expected, along and cross track errors are larger. SGM100h and LP100K perform at a similar level, with LP100K sometimes performing better than SGM100h. On the other hand, SGM100h seems to be slightly more consistent overall, showing less variations. This is especially so for one overlap around July 13 when compared to LP100K. Similar results can also be seen for the cross-track direction, and this is connected to a rather specific orbital geometry: during that period, LP was in a so-called edge-on orbit, where the satellite flew over the deep farside, namely, over the Korolev/Dirichlet-Jackson combination over the far side, which appear as strong, circular anomalies in the map of SGM100h. It seems likely that SGM100h has the ability to perform better for such an orbit due to the inclusion of farside tracking data, but care should be taken not to over-interpret the results, because as is shown in Figure 2, the northern part of the farside still shows data gaps. Nevertheless, a similar coverage is achieved two weeks later, due to the natural rotation of the orbital plane, and for this arc, around 27 July the SELENE models again outperform LP100K in both along and cross-track, with the cross-track outlier for LP100K less pronounced as for the 13 July arc. Another edge-on orbit configuration occurs at 1 July but for this arc the ground track does not go directly over Korolev/Dirichlet-Jackson.

[58] Face-on geometries, with the satellite flying along the limbs of the Moon, occur 7 days from edge-on geometries, and here SGM90d performs better than both LP100K and its successor SGM100h, for the along-track direction. Even though 4-way data during a face-on geometry provide additional constraints to standard 2-way data (which follow the line-of-sight from tracking station to satellite), differences between processing of the data for SGM90d and SGM100h might have lead to different performances. Rstar arcs for SGM100h were longer, but during face-on geometries this might have had some degrading influences, especially since at times, standard 2-way tracking to Rstar was less. The inclusion of longer stretches of differential VLBI tracking in future solutions might mitigate this effect.

[59] Concluding, orbit overlap analysis shows similar performances for the models, with a total overlap consistency of less than 50 m, and less than 1 m in the radial direction. Inclusion of farside tracking data improves the performance of the SELENE models for edge-on configurations.

4.6. GM and k_2

[60] We obtained 4902.80212 ± 0.00013 km^3/s^2 as the GM, which is compared with 4902.80108 ± 0.00008 km^3/s^2 for LP150Q. The formal errors need to be multiplied by 5 to be consistent with each other. The tidal Love number solution for SGM100h is k_2 = 0.0240 ± 0.0015. Note that the k_2 uncertainty is ten times the formal error following *Konopliv et al.* [2001] and considering the possibly too optimistic formal error for the low-degree gravity coefficients. The k_2 value is close to 0.0244 ± 0.0008, one of the results from reanalysis of the historical tracking data by *Goossens and Matsumoto* [2008] which is obtained without estimating empirical acceleration for LP (similar processing to this study), and to 0.0248 ± 0.003 for LP150Q (A. Konopliv, personal communication, 2009). Both the uncertainties are again ten times the formal errors. The three satellite-derived k_2 estimates are consistent with each other within a scatter of about 3%. *Goossens and Matsumoto* [2008] showed, however, that even with the same historical data set, application of the empirical accelerations changes

the k_2 value by 0.0031, and that the solutions are also affected by the data weights. Furthermore, the independent Lunar Laser Ranging (LLR) data analysis gives the recent k_2 solution of 0.0199 ± 0.0025 [*Williams et al.*, 2009], with which the k_2 formal error of SGM100h needs to be multiplied by more than ten to be consistent. The differences between the satellite-based and the LLR-based estimates are still about 20% of k_2 value, whereas it is required to achieve a 5% of k_2 uncertainty in order to discuss the presence of an iron core [*Wieczorek et al.*, 2006]. The k_2 derivation from the LLR data requires internal structure modeling, and the k_2 estimate has been steadily going down (e.g., *Dickey et al.* [1994] reported $k_2 = 0.0302 \pm 0.0012$), depending on different modeling such as taking core ellipticity into account and introducing a solid inner core. The satellite-based estimates come from the temporal change of the gravitational potential, independent of a model for the internal structure, but the sensitivity is small because of the 1 order of magnitude smaller lunar k_2 value compared with that of the Earth. Improvements in the satellite-based estimates will come from larger sensitivity with longer satellite arcs and precise VLBI data. Therefore, for discussions on the lunar deep interior, it is still necessary to further refine and stabilize the Love number estimation, to which the SELENE differential VLBI data and a better modeling of nonconservative forces are expected to contribute.

5. Summary

[61] We have described in detail the SELENE lunar gravity mission, including the tracking data acquisition and our methodology to derive a new spherical harmonic model of the lunar gravity field (SGM100h), with emphasis on the 4-way Doppler data which have filled in most of the tracking data gap in the farside. As a result, SGM100h, complete to degree and order 100, has been developed by incorporating the historical tracking data of the Lunar Orbiters, the Apollo subsatellites, the Clementine, the SMART-1 and the Lunar Prospector, and 14.2 months of SELENE Doppler and range data including all the usable 4-way Doppler data. Compared to LP100K, SGM100h reveals greater detail in the farside free-air gravity anomalies which have larger correlations with the SELENE, laser-altimeter-derived, topography. The RMS coefficient power degree variances in the farside are about twice as large as those in nearside beyond degree 35. With the farside data coverage achieved, even with a small data gap still remaining in the northern hemisphere, it is possible to obtain a realistic gravity expansion up to degree and order 70 without any a priori constraint. Judging from the power spectrum of the unconstrained solution, a Kaula type constraint with $\beta = 3.6$ is reasonable, at least it does not suppress the true coefficient power. The 4-way Doppler data significantly contribute to reduce the projected error in the farside. The free-air gravity anomaly error averaged over the farside is reduced from 55 mGal for LP100K down to 35 mGal for SGM100h, with a more homogeneous selenographical error distribution for the latter. The South Pole-Aitken basin, which is located at the region with the densest 4-way Doppler data, is investigated and its elliptical signature has been identified from the viewpoint of the Bouguer gravity anomaly. The SGM100h coefficients below degree and order 70 are determined by the observations with contribution factors larger than 80 percent. Although it is demonstrated that most low-degree terms are determined from the data, the conventional Kaula-type constraint might still affect their determination. Careful studies on the influence of regularization will benefit future refinements. Even without including LP extended mission data, overall orbit determination performance of SGM100h is at a similar level as LP100K, and some improvements are observed for edge-on configuration in which a satellite experiences the farside gravity. In global sense, the model can be confidently used for geophysical interpretation through degree and order 70, although the low-degree coefficients and k_2 Love number still need to be further refined and stabilized, to which SELENE differential VLBI data are expected to contribute. Lunar gravity field models with finer spatial resolution and with smaller uncertainties will be achieved by U.S. GRAIL mission [*Zuber et al.*, 2008] to be launched in 2011.

[62] **Acknowledgments.** The authors appreciate the contribution of all the engineers of NEC/Toshiba Space Systems Ltd. (NTS), Nippon Antenna Co. Ltd., and Nippi Corporation who diligently developed the onboard instruments and subsatellites. We also express thanks to the entire staff of the SELENE mission. The gravity experiments conducted during the SELENE mission would never have been achieved without the prominent expertise and profound knowledge of Fumio Fuke, an NTS engineer who passed away 2 months after the mission was launched. We express sincere thanks to him for his contributions to science and mourn his passing and the loss it entails for Japanese space development. We are thankful to two anonymous reviewers who helped improving our manuscript. We used the Generic Mapping Tools (GMT) software [*Wessel and Smith*, 1991] for drawing the figures. Our localized spherical harmonic analyses were performed using the freely available software archive SHTOOLS (available at http://www.ipgp.jussieu.fr/wieczor/SHTOOLS/SHTOOLS.html).

References

Akim, E. L. (1966), Determination of the gravitational field of the Moon from the motion of the artificial satellite "Lunar-10," *Dokl. Akad. Nauk SSSR*, *170*, 799–802.

Araki, H., et al. (2009), Lunar global shape and polar topography derived from Kaguya-LALT laser altimetry, *Science*, *323*, 897–900.

Bills, B. G., and A. J. Ferrari (1980), A harmonic analysis of lunar gravity, *J. Geophy. Res.*, *85*, 1013–1025.

Dickey, J. O., et al. (1994), Lunar laser ranging: A continuing legacy of the Apollo program, *Science*, *265*, 482–490.

Floberghagen, R. (2002), *Lunar gravimetry: Revealing the far-side*, *Astrophys. Space Sci. Libr.*, vol. 273, Kluwer Acad. Publ., Dordrecht, Netherlands.

Floberghagen, R., J. Bouman, R. Koop, and P. Visser (1999), On the information contents and regularisation of lunar gravity field solutions, *Adv. Space Res.*, *23*, 1801–1807.

Garrick-Bethell, I., and M. T. Zuber (2009), Elliptical Structure of the Lunar South Pole-Aitken Basin, *Icarus*, *204*, 399–408, doi:10.1016/j.icarus.2009.05.032.

Goossens, S., and K. Matsumoto (2007), Lunar satellite orbit determination analysis and quality assessment from Lunar Prospector tracking data and SELENE simulations, *Adv. Space Res.*, *40*, 43–50, doi:10.1016/j.asr.2006.12.008.

Goossens, S., and K. Matsumoto (2008), Lunar degree 2 potential Love number determination from satellite tracking data, *Geophys. Res. Lett.*, *35*, L02204, doi:10.1029/2007GL031960.

Han, S.-C. (2008), Improved regional gravity fields on the Moon from Lunar Prospector tracking data by means of localized spherical harmonic functions, *J. Geophys. Res.*, *113*, E11012, doi:10.1029/2008JE003166.

Han, S.-C., E. Mazarico, and F. G. Lemoine (2009), Improved nearside gravity field of the Moon by localizing the power law constraint, *Geophys. Res. Lett.*, *36*, L11203, doi:10.1029/2009GL038556.

Hanada, H., et al. (2008), VLBI for Better Gravimetry in SELENE, *Adv. Space Res.*, *42*, 341–346, doi:10.1016/j.asr.2007.11.003.

Imamura, T., K. Oyama, T. Iwata, Y. Kono, K. Matsumoto, Q. Liu, H. Noda, Y. Futaana, and A. Nabatov (2008), The possibility of studying the lunar ionosphere with the SELENE radio science experiment, *Earth Planets Space*, *60*, 387–390.

Iwata, T., M. Takahashi, N. Namiki, H. Hanada, N. Kawano, K. Heki, K. Matsumoto, and T. Takano (2001), Mission Instruments for Lunar Gravity Measurements using SELENE Sub-satellites, *J. Geod. Soc. Jpn.*, *47*, 558–563.

Kaula, W. M. (1963), The investigation of the gravitational fields of the moon and planets with artificial satellites, *Adv. Space Sci. Technol.*, *5*, 210–230.

Kaula, W. M. (1966), *Theory of Satellite Geodesy*, Blaisdell, Waltham, Mass.

Kikuchi, F., et al. (2009), Picosecond accuracy VLBI of the two subsatellites of SELENE (KAGUYA) using multifrequency and same beam methods, *Radio Sci.*, *44*, RS2008, doi:10.1029/2008RS003997.

Kobayashi, H., et al. (2003), VERA Project, in *New Technologies in VLBI*, *ASP Conf. Ser.*, vol. 306, edited by Y. C. Minh, pp. 367, Astron. Soc. of the Pac., San Francisco, Calif.

Konopliv, A. S., and R. N. Sjogren (1994), Venus spherical harmonic gravity model to degree and order 60, *Icarus*, *112*, 42–54.

Konopliv, A. S., and D. N. Yuan (1999), Lunar Prospector 100th degree gravity model development, *Lunar Planet. Sci. Conf.*, *XXX*, Abstract 1067.

Konopliv, A. S., W. L. Sjogren, R. N. Wimberly, R. A. Cook, and A. Vijayaraghavan (1993), A high resolution lunar gravity field and predicted orbit behavior, presented at the AAS/AIAA Astrodynamics Specialist Conference, Victoria, B. C., Canada, 16–19 August.

Konopliv, A. S., A. B. Binder, L. L. Hood, A. B. Kucinskas, and J. G. Williams (1998), Improved gravity field of the Moon from Lunar Prospector, *Science*, *281*, 1476–1480.

Konopliv, A. S., S. W. Asmar, E. Carranza, W. L. Sjogren, and D. N. Yuan (2001), Recent gravity models as a result of the lunar prospector mission, *Icarus*, *150*, 1–18.

Lemoine, F. G. R., D. E. Smith, M. T. Zuber, G. A. Neumann, and D. D. Rowlands (1997), A 70th degree lunar gravity model (GLGM-2) from Clementine and other tracking data, *J. Geophys. Res. 102*, 16,339–16,359, doi:10.1029/97JE01418.

Lemoine, F. G., D. E. Smith, D. D. Rowlands, M. T. Zuber, G. A. Neumann, D. S. Chinn, and D. E. Pavlis (2001), An improved solution of the gravity field of Mars (GMM-2B) from Mars Global Surveyor, *J. Geophys. Res.*, *106*, 23,359–23,376, doi:10.1029/2000JE001426.

Liu, Q., S. Tsuruta, K. Asari, J. Ping, F. Kikuchi, K. Matsumoto, and N. Kawano (2004), New method of measuring phase characteristics of antenna using Doppler frequency measurement technique, *IEEE Trans. Antennas Propag.*, *52*(12), 3312–3318.

Liu, Q., et al. (2010), Effect of phase pattern of antennas onboard flying spin satellites on doppler measurements for lunar gravity field, *IEEE Trans. Aerosp. Electron. Syst.*, in press.

Luthcke, S., J. Marshall, S. Rowton, K. Rachlin, C. Cox, and R. Williamson (1997), Enhanced radiative force modelling of the tracking and data relay satellites, *J. Astronaut. Sci.*, *45*(3), 349–370.

Matsumoto, K., H. Hanada, N. Namiki, T. Iwata, S. Goossens, S. Tsuruta, N. Kawano, and D. Rowlands (2008), A simulation study for anticipated accuracy of lunar gravity field model by SELENE tracking data, *Adv. Space Res.*, *42*, 331–336, doi:10.1016/j.asr.2007.03.066.

Marshall, J., and S. Luthcke (1994), Modeling radiation forces acting on TOPEX/Poseidon for precision orbit determination, *J. Spacecr. Rockets*, *31*(1), 99–105.

Milani, A., A. M. Nobili, and P. Farinella (1987), *Non-gravitational Perturbations and Satellite Geodesy*, IOP Publ., Bristol, England.

Montenbruck, O., and E. Gill (2000), *Satellite Orbits*, Springer, Heidelberg.

Muller, P. M., and W. L. Sjogren (1968), Masscons: Lunar mass concentrations, *Science*, *161*, 680–684.

Namiki, N., et al. (1999), Selenodetic experiments of SELENE: Relay subsatellite, differential VLBI, and laser altimeter, *Adv. Space Res.*, *23*, 1817–1820.

Namiki, N., et al. (2009), Far side gravity field of the Moon from four-way Doppler measurements of SELENE (Kaguya), *Science*, *323*, 900–905.

Pavlis, D. E., S. Poulose, and J. J. McCarthy (2009), GEODYN operations manuals, contractor report, SGT Inc., Greenbelt, Md.

Ping, J., Y. Kono, A. Tsuchiya, and N. Kawano (2000), Effects on Doppler frequency measurement due to the spin and a phase delay pattern of an antenna onboard a spacecraft, *J. Geod. Soc. Jpn.*, *46*, 187–202.

Sugano, T., and K. Heki (2004), High resolution lunar gravity anomaly map from the lunar prospector line-of-sight acceleration data, *Earth Planets Space*, *56*, 81–86.

Ullman, R. (2002), SOLVE program, users guide, *Contract nas5-31760*, Raytheon STX Corp., Lanham, Md.

Watts, A. B. (2001), *Isostasy and Flexure of the Lithosphere*, pp. 458, Cambridge Univ. Press, New York.

Wessel, P., and W. H. F. Smith (1991), Free software helps map and display data, *Eos. Trans. AGU*, *72*, 441.

Wieczorek, M. A., et al. (2006), The constitution and structure of the lunar interior, *Rev. Mineral. Geochem.*, *60*, 221–364, doi:10.2138/rmg.2006.60.3.

Wilhelms, D. E., J. F. McCauley, and N. J. Trask (1987), The geologic history of the Moon, *U.S. Geol. Surv. Prof. Pap., 1348*, 302 pp.

Williams, J. G., D. H. Boggs, and W. M. Folkner (2008), DE421 lunar orbit, physical librations, and surface coordinates, *JPL Mem. IOM 335-JW, DB, WF-20080314-001*, 14 March, Jet Propulsion Lab., Calif. Inst. of Technol., Pasadena, Calif. (Available at ftp://ssd.jpl.nasa.gov/pub/eph/planets/ioms/de421_moon_coord_iom.pdf)

Williams, J. G., D. H. Boggs, and J. T. Ratcliff (2009), A larger lunar core?, *Lunar Planet. Sci.*, *XXXX*, Abstract 1452.

Zuber, M. T., et al. (2008), Outstanding questions on the internal structure and thermal evolution of the Moon and future prospects from the GRAIL mission, *Lunar Planet. Sci.*, *XXXIX*, Abstract 1074.

S. Goossens, H. Hanada, Y. Ishihara, F. Kikuchi, K. Matsumoto, and H. Noda, RISE Project, National Astronomical Observatory of Japan, Mizusawa, Oshu, Iwate 023-0861, Japan. (matumoto@miz.nao.ac.jp)

T. Iwata, Japan Aerospace Exploration Agency, Sagamihara, Kanagawa 229-8510, Japan.

N. Kawano and Q. Liu, Shanghai Astronomical Observatory, Shanghai 200030, China.

F. G. Lemoine and D. D. Rowlands, Planetary Geodynamics Laboratory, Solar System Exploration Division, NASA Goddard Space Flight Center, Greenbelt, MD 20771, USA.

N. Namiki, Planetary Exploration Research Center, Chiba Institute of Technology, Narashino, Chiba 275-0016, Japan.